Aalto University
School of Electrical Engineering
Degree Programme in Electronics and Electrical Engineering

Joonas Holmi

# Determining the number of graphene layers by Raman-based Si-peak analysis

Master's Thesis
Espoo, 18.4.2016

Supervisor: Prof. Harri Lipsanen
Advisor: Dr. Juha Riikonen

Aalto University
School of Electrical Engineering
Degree Programme in Electronics and Electrical Engineering

ABSTRACT OF MASTER'S THESIS

| | | | |
|---|---|---|---|
| **Author:** | Joonas Holmi | | |
| **Title:** | Determining the number of graphene layers by Raman-based Si-peak analysis | | |
| **Date:** | 18.4.2016 | **Pages:** | 69 |
| **Major:** | Nanotechnology | **Code:** | S341-3 |
| **Supervisor:** | Prof. Harri Lipsanen | | |
| **Advisor:** | Dr. Juha Riikonen | | |

Raman spectroscopy is the most used and versatile tool in the material characterization of graphene. Wide array of structural information, such as defects, doping, number of layers, stacking order and strain, are simultaneously encompassed in the Raman spectrum. This work focused in determining the number of layers using Raman. The main problem with the current Raman methods using graphene spectrum is that they often saturate and sense the stacking order, being limited to only few-layers of ABA-stacked graphene. This is especially problematic when analysing multilayer chemical vapour deposited graphene, which is often unintentionally randomly stacked.

In this work, the Si-peak analysis was developed to address these fundamental limitations. It relies on the silicon peak originating from the substrate, for which the absorption relates to the number of graphene layers. The normalized Si-peak intensity is obtained simultaneously with the Raman analysis of graphene on $SiO_2$/Si–substrate. Model was tested using pristine graphene on 285 nm and 365 nm oxide, bare 0–400 nm oxide and random stacking. The calculated number of layers agreed with the thickness references and were insensitive to graphene properties unlike other tested Raman-based methods. Model was also robust against random stacking, even near the resonant rotational angle, where graphene Raman band changes become difficult to predict. The Si-peak analysis, being virtually immune to variation within graphene, is a promising non-destructive widely applicable method to determine the number of even arbitrarily stacked graphene layers up to 100.

| | |
|---|---|
| **Keywords:** | graphene, Raman spectroscopy, number of layers, thickness, Si-peak |
| **Language:** | English |

Aalto-yliopisto
Sähkötekniikan korkeakoulu
Elektroniikan ja sähkötekniikan koulutusohjelma

DIPLOMITYÖN
TIIVISTELMÄ

| | | | |
|---|---|---|---|
| **Tekijä:** | Joonas Holmi | | |
| **Työn nimi:** | Grafeenin kerroslukumäärän määrittely Raman-pohjaisella Si-piikin analyysilla | | |
| **Päiväys:** | 18.4.2016 | **Sivumäärä:** | 69 |
| **Pääaine:** | Nanotekniikka | **Koodi:** | S341-3 |
| **Valvoja:** | Prof. Harri Lipsanen | | |
| **Ohjaaja:** | Tkt. Juha Riikonen | | |

Raman-spektroskopia on käytetyin ja monipuolisin työkalu grafeenin karakterisoinnissa. Laaja määrä tietoa rakenteesta, kuten kidevirheet, varauksenkuljettajatiheys, kerroslukumäärä, kerrosorientaatio ja jännitys, voidaan selvittää samasta Raman-spektristä. Tämä työ keskittyi kerroslukumäärien määrittelyyn Ramanilla. Merkittävin ongelma Raman-menetelmissä, jotka hyödyntävät grafeenin spektriä, on se, että ne usein saturoituvat ja ovat herkkiä kerrosorientaatiolle, rajoittuen muutamakerroksiseen ABA-kerrosorientoituun grafeeniin. Tämä on erityisen ongelmallista, kun analysoidaan kaasufaasipinnoituksella tuotettua monikerroksista grafeenia, joka on usein satunnaisesti kerrosorientoitunutta.

Tässä työssä kehitettiin Si-piikin analyysi vastaamaan näihin perustavanlaatuisiin rajoituksiin. Piistä tulevan Raman-signaalin voimakkuus riippuu kerroslukumäärästä. Normalisoitu Si-piikin intensiteetti mitataan samanaikaisesti osana grafeenin Raman-spektriä $SiO_2$/Si–substraatilla. Uutta mallia testattiin exfolioidulla grafeenilla, jonka alla on 285 nm ja 365 nm oksidia, paljaalla 0–400 nm:n oksidilla ja satunnaisella kerrosorientaatiolla. Mallin perusteella saadut kerroslukumäärät vastasivat vertailuarvoja, eivätkä olleet herkkiä grafeenin ominaisuuksille muiden Raman-pohjaisten menetelmien tavoin. Malli toimii myös satunnaisen kerrosorientaation tapauksessa, jopa lähellä resonanssia olevaa kiertokulmaa, jossa grafeenin Raman-piikkien muutokset ovat vaikeasti ennustettavissa. Työssä kehitetty Si-piikin intensiteettiin perustuva analyysi on lupaava näytteelle haitaton ja laajalti käyttökelpoinen menetelmä jopa mielivaltaisesti kerrosorientoituneen grafeenin paksuusmäärittelyyn aina sataan kerrokseen asti.

| | |
|---|---|
| **Asiasanat:** | grafeeni, Raman-spektroskopia, kerroslukumäärä, paksuus, Si-piikki |
| **Kieli:** | Englanti |

# Acknowledgements

My deepest gratitude to my advisor Dr. Juha Riikonen for the patience, the sincerity, the support, the humor and the conversations over the years. My wife and I are very thankful to you and my supervisor Prof. Harri Lipsanen for the patience, as the whole process took very long, and the possibility to work on the interesting subject. I am grateful to my colleague Dr. Kim Wonjae for training me in Raman spectroscopy of graphene and providing me important Raman data on the randomly stacked multilayer CVD graphene. My sincere appreciation to all my colleagues in the graphene group.

My heart is profoundly grateful for my best friend, heart companion and gorgeous wife Susanna Holmi! My earnest appreciation to my dear friends Mikael Isoaho and Mikael Rönkkö for the time, the prayers and the brotherhood. My love to my mother Marja-Vuokko Mäkinen for the wholehearted prayers and the immense encouragement, and my father Aulis Mäkinen for the father-son time. My gratitude to my family and friends for the support, my study psychologist Minna Nevala for the tools, Virpi Palmgren for the thesis writing course and Prof. Esa Saarinen for the systems thinking course.

The last but certainly not the least, all glory to the Lord of Lords, the Son of God and my Saviour Lord Jesus Christ! I am eternally grateful for the finished work! At the most painful moments and the deepest sorrows, His Grace, Love and Power lifted me up! By His Grace, I know all of you people. By His Love, I met my wife during the three years of working on this subject. By His Power, I was able to complete this thesis. For example, the data processing before the Si-peak analysis greatly benefited from the MRLCM–algorithm (described in Section 4.2.3), which He put to my heart. I am certain that nothing is impossible to God! May this work inspire you!

With utmost sincerity!

Espoo, 18.4.2016

Joonas Holmi

# Symbols and Abbreviations

| | |
|---|---|
| 2-D | Two-dimensional |
| 2D | The 2nd main Raman band of graphene at ∼2680 $cm^{-1}$ |
| ABA | Bernal stacking order |
| ABC | Rhombohedral stacking order |
| AFM | Atomic force microscopy |
| BLG | Bi-layer graphene |
| CVD | Chemical vapour deposition |
| Cu | Copper |
| G | The 1st main Raman band of graphene at ∼1580 $cm^{-1}$ |
| FLG | Few-layer graphene |
| FWHM | Full width at half maximum |
| I | The intensity of specified Raman peak |
| Pos | The spectral position of specified Raman peak |
| PMMA | Poly(methyl methacrylate) |
| PTCM | Plane tilt correction by multiplication |
| MRLCM | Median ratio line correction by multiplication |
| NA | Numerical aperture of a lens system |
| NaN | Not-a-number |
| N-LG | $N$-layer graphene. |
| $R^2$ | A coefficient of determination |
| Ratio–I | The intensity ratio of specified Raman peaks |
| RND | Random stacking order |
| SEM | Scanning electron microscopy |
| Shape | The spectral shape of Raman peak |
| Si | Silicon. Can denote the main Raman band of Si at ∼520 $cm^{-1}$ |
| $SiO_2$ | Silicon oxide |
| SPR | Surface plasmon resonance |
| SLG | Single-layer graphene |
| SSE | A sum of squared errors |
| TEM | Transmission electron microscopy |

# Contents

# List of Figures

# Chapter 1

# Introduction

Graphene, the two-dimensional (*2-D*) allotrope of carbon, is the first one-atom thick material discovered. It has unique electrical, optical, mechanical and thermal properties. For instance, while it is highly transparent and bendable as plastic, it also conducts electricity as well as copper. Mechanically exfoliated single-layer graphene (*SLG*) obtained from graphite is pristine, which is useful in the experimental research. However, other fabrication methods have been developed to access industrial-scale manufacturing. Currently chemical vapour deposition (*CVD*) is the best candidate to obtain large-area SLG. Properties of the synthesized graphene are often characterized using Raman spectroscopy. Those are evaluated by analysing its Raman fingerprints, for example the G-, 2D- and D-peak intensities. As the Raman spectrum encompasses wide array of structural information, it can be used to determine the doping, the stacking order, the strain or the number of layers.

Main focus in this work was in determining the number of graphene layers by Raman spectroscopy. While there are several non-Raman methods to determine the number of layers, each of them require extra work beside the Raman measurements. In addition, most of them are not applicable beyond several layers. Although a low throughput method, atomic force microscopy (*AFM*), is often used to confirm the number of layers, even though it is troubled by an anomalous offset for graphene. The Raman-based methods are of particular interest because the required information for analysis is already included within the measured Raman spectra. However, the main problem in using the Raman methods based on the graphene spectrum is that there are several factors that limit their use. First of all, many Raman fingerprints of graphene saturate after 5 layers, becoming useless in determining the larger number of layers. In addition, most of the fingerprints are sensitive to the variation in graphene, such as the stacking order and the defects, and the substrate below via the interference phenomenon. Stacking order sensitivity

is especially problematic when analysing multilayer CVD graphene, which often contains unintentional randomly stacked layers. Consequently, it is paramount to establish straight-forward widely applicable method.

To address these fundamental limitations, the Si-peak analysis is introduced and derived in this work. It relies on the main Raman Si-peak intensity, which originates from $SiO_2$/Si–substrate, on which graphene has often been transferred. The emitted Si-peak intensity then propagates through graphene and its absorption is related to the number of layers. As the Si-peak analysis does not rely on any Raman fingerprint of graphene, it is virtually immune to the variation within the graphene structure, solving the problems related to analysis based on graphene Raman spectra. Moreover, the main Si-peak intensity is strong and obtained simultaneously with the Raman analysis of graphene on $SiO_2$/Si–substrate. Unlike most other methods, the Si-peak analysis is applicable up to 100 layers, being a promising alternative to AFM.

The layout of this work is as follows: The background is considered further in Chapter 2. The experimental methods used in this work are introduced in Chapter 3. The Si-peak analysis, including all the data processing involved and the Si-peak intensity model, is described and derived in Chapter 4. The results on the Si-peak analysis are presented and discussed in Chapter 5. The key findings of this work are summarized in Chapter 6.

# Chapter 2

# Background

## 2.1 Introduction to Graphene

Graphene is the first experimentally verified one atom thick thermodynamically stable 2-D material, opposing the initial theoretical predictions [33]. It was discovered by Andre Geim and Konstantin Novoselov in 2004, what later awarded them the Nobel Prize in 2010 [80]. Graphene lattice consists of $sp^2$-hybridized carbon atoms arranged in a hexagonal honeycomb with bond length of 0.142 nm. Naturally occurring graphite, used as a composite material in the pencil cores for centuries, is a stack of graphene layers with interlayer distance of about 0.335 nm [3].

The numerous properties and characteristics of pristine graphene are spectacular and unique [19, 30, 80]. It withstands stretching, is light-weight ($7.7 \cdot 10^{-4}$ $gm^{-2}$) and a hundred times stronger than steel [59]. It has high surface/volume ratio, electron mobility ($2 \cdot 10^5$ $cm^2V^{-1}s^{-1}$ [4]) and thermal conductivity ($5{\cdot}10^3$ $WmK^{-1}$ [2]). Two-dimensionality makes it highly flexible and transparent with 2.3 % absorption of visible light [74]. It is impermeable to all gases and liquids [45]. The electronic band structure of graphene is intrinsically metallic. For instance, doped [22] or gated [107] bi-layer graphene ($BLG$) and graphene nanoribbons with armchair edges [75] can be semiconducting. The optical properties are also tunable via electrical gating [107]. A more exotic features include the ability to self-repair [105] and Hofstadter's butterfly fractal pattern for electron motion in magnetic field [104]. Overall, graphene has many extraordinary properties compared to those of the standard materials. Its simple structure and unique properties have made it an experimental testbed for many physical theories [19, 30].

The unique properties of graphene enable high frequency, flexible and transparent electronics [30]. It may be used as a transparent conductive heat

spreading layer to allow the fabrication of higher efficiency solar cells, CCDs and LEDs [30]. Furthermore, graphene devices may be used in terahertz [100] and radio-frequency applications [95]. Electronic band structure may be utilized in spintronics [37] and valleytronics [88]. Ultrathin metallic graphene may be used to build new generation batteries and supercapacitors [51]. Other exciting applications include membranes [55], water desalination [93], hydrogen storage [45], DNA sequencing [40], one-molecule sensitivity [90] and corrosion protection [85]. Moreover, graphene may be combined with other 2-D materials to form nanocomposites [30] and heterostructures [30, 80].

Initially graphene was produced from graphite by mechanical exfoliation using tape [80]. This discovery has led to the development of various fabrication methods [30], such as CVD [20], growth on silicon carbide [28] and liquid phase exfoliation [62]. Although the largest mechanically exfoliated pristine graphene flakes reported are millimetre-scale [32], the method is not scalable and not for industry. Other fabrication methods typically produce polycrystalline graphene with intrinsic imperfections such as functional groups, grain boundaries, unintentional multilayer growth and vacancy defects. These imperfections limit access to the exceptional properties of pristine graphene. Currently the best candidate to synthesize large-area single-crystalline monolayer graphene is CVD, for which a single crystalline inch-scale growth [99] and a polycrystalline 30-inch-scale growth [1] has been reported. While these are impressive technological advances, more optimization effort is required to guarantee large-scale production without at the expense of graphene quality. Optimized characterization is an obvious prerequisite for determining the material quality. Synthesized graphene is tested for a number of factors, such as defects, polycrystallinity and the number of layers, by wide variety of methods. The main focus in this work is the determination of the number of graphene layers.

## 2.2 Characterizing the Number of Layers

### 2.2.1 Non-Raman Methods

Mainstream non-Raman based methods to estimate the number of graphene layers are listed with their applicability, advantages and disadvantages in Table 2.1. They are applicable nearly completely regardless the stacking order or the defect density of graphene. Optical methods may fail for the random-stacked graphene at rotational angles of 10–15°, where an angle-dependent optical absorption peak is within the visible spectrum [71, 87]. This non-exhaustive list includes following methods and descriptions in alphabetical

order: 1) AFM, which excels at sample topography imaging. 2) Optical color difference microscopy, which requires full color images to calculate the number of layers. 3) Optical contrast microscopy, which estimates the number of layers via the relative differences in intensities. 4) Optical transmittance microscopy, which evaluates the thickness via the measured transmitted light. 5) Scanning electron microscopy (*SEM*), which is a destructive high resolution imaging method useful for few-layer graphene (*FLG*). 6) Surface plasmon resonance (*SPR*), which is linear for graphene on a carefully prepared special SPR-activated substrate. 7) Transmission electron microscopy (*TEM*), which performs an exact crystallography for FLG at atomic resolution.

Table 2.1: Non-Raman methods, which may be used to determine the number of graphene layers almost completely regardless the stacking order or the defect density. Optical methods may cease working at a narrow range of random stacking orders, for which the optical absorption is locally enhanced.

| **Method** | **Range** | **Pros** | **Cons** | **Refs.** |
|---|---|---|---|---|
| AFM | 3–$\infty$ | Accurate surface topography. Sub-nm resolution. Direct measure. | Slow. Sub-mm scan area. Anomalous offset for graphene. Artefacts. | [77] |
| Optical color difference | 1–10 | Fast. Camera only. Any substrate. Large area. Visual correspondence. | Complex model. Needs lamp spectrum and uniform lightning. | [11, 31, 57, 72] |
| Optical contrast | 1–10 | Fast. Intensity only. Simple model. Large area. | Needs reference at bare substrate, uniform lightning, optimal substrate. | [50, 60, 79] |
| Optical transmittance | 1–7 | Transmittance only. Linear relationship. | Needs to be suspended or on transparent substrate. | [1, 47] |
| SEM | 1–8 | Fast. Large area scan. Linear beyond 2 layers. | Needs calibration sample, low voltage and reference. Destroys. | [44, 54] |
| SPR | 1–50 | Linear relationship up to 50 layers. Non-intrusive. Simple model. | Needs large sample on special substrate. Surface roughness sensitive. | [13, 26] |
| TEM | 1–3 | Exact crystallography. Stacking order and defect sensitive. | Needs to be suspended or on thinned substrate. Very slow. Destroys. | [15, 73, 84] |

### 2.2.2 Raman Methods

Raman spectroscopy has widely been used to characterize various properties of pristine or synthesized graphene: crystallographic orientation [70], defects [24, 63], doping [10, 21], edges [9, 103], functional groups [24, 27], isotope

concentration [7], number of layers [47, 61, 78], stacking order [16, 47, 78], strain [102] and temperature [6, 25]. The attracting aspect of Raman spectroscopy is that for each measurement it collects a spectrum, in which all this information is included. The measured spectrum can then be carefully analysed to access various information on graphene.

Raman spectrum of SLG is featured by two main peaks, G and 2D (or G'), located at $\sim$1580 cm$^{-1}$ and $\sim$2680 cm$^{-1}$, respectively, using 532 nm laser excitation. Other bands of interest include C at $\sim$40 cm$^{-1}$, N at $\sim$1500 cm$^{-1}$, M at $\sim$1750 cm$^{-1}$ and G* at $\sim$2450 cm$^{-1}$, and their combination modes (*CMs*) and layer-breathing modes (*LBMs*) [49, 64, 78, 94]. Many of these are sensitive to the number of graphene layers and the stacking order. Moreover, graphene with defects shows additional D and D' bands located at $\sim$1350 cm$^{-1}$ and $\sim$1620 cm$^{-1}$, respectively. The currently accepted understanding is that the G band originates from one-phonon Raman scattering process associated with the doubly degenerate in-plane transverse optic (*iTO*) and longitudal optic (*LO*) phonon modes at the Brillouin zone. Many other bands, including the 2D band, are attributed to second-order phonon processes according to the double resonance theory [29, 67], which is the theoretical framework relied on in this work. However, an alternative explanation has recently been presented: Kramers–Heisenberg–Dirac theory, which is incompatible with the double resonance theory [41].

Previous work on Raman based methods for determining the number of graphene layers are presented in Table 2.2. However, the list is in no way exhaustive and its purpose is to provide an overview on perhaps the most commonly used methods. All methods are guaranteed to apply to Bernal (*ABA*) stacked *N*-layer graphene (*N-LG*). However, if the method is useful for rhombohedral (*ABC*) or random (*RND*) stacking orders, then those are specified in the range column. The used experimental setups were included to give insight on the scope of the previous research. Laser excitation wavelengths span across 784.7 nm (1.58 eV), 632.6 nm (1.96 eV), 532.1 nm (2.33 eV), 514.5 nm (2.41 eV), 488.1 nm (2.54 eV) and 441.2 nm (2.81 eV). Numerical aperture (*NA*), relevant in the context of this work, was often specified for 100$\times$ lens. In addition to the previously listed Raman bands, the main Si-peak at $\sim$520 cm$^{-1}$ and the Rayleigh peak at $\sim$0 cm$^{-1}$ are also included in this table. Different aspects of peaks were considered: the peak-to-peak intensity ratio (*Ratio–I*), the peak spectral shape (*Shape*), the peak intensity (*I*), the peak spectral position (*Pos*), the full width at half maximum (*FWHM*) of the peak. However, the methods based on the peak area (*A*) or the peak-to-peak area ratio (*Ratio–A*) were not listed as they can often be calculated using the relation for Lorentzian peaks: $\mathrm{A} = \frac{\pi}{2} \cdot \mathrm{I} \cdot \mathrm{FWHM}$. This notation is used hereafter.

The fundamental limitations of each graphene Raman spectrum based methods, such as the sensitivity to the oxide thickness or the stacking order, are shown in Table 2.2. For example, the G- and 2D-peaks intensities, I(G) and I(2D), (and areas, A(G) and A(2D)) have been reported to change as a function of the oxide thickness and the NA due to the inferference phenomenon [101], and the rotational angle of the RND-stacked graphene due to the angle dependent Van Hove singularities [39, 52, 71]. Moreover, it is reported that many Raman peaks of graphene are sensitive to the ABC-stacking order [78], seen as change in Shape, Pos and FWHM. Also, I(G) and I(2D) are slightly sensitive to the ABC-stacked graphene. Although not mentioned in Table 2.2, all Raman peaks show dispersion and depend on the laser excitation energy [78]. This multitude of dependencies on the graphene properties limit the use of graphene Raman spectrum based methods in determining the number of layers.

The Si-peak analysis, also denoted Ratio–I($Si_G$, $Si_0$), was developed to address these limitations. The intensities, I($Si_G$) and I($Si_0$), represent the main Si-peak intensities originating from the substrate below propagated through graphene and no graphene, respectively. The I($Si_G$) absorption is related to the number of graphene layers. The Si-peak analysis is carefully described and rigorously derived in Chapter 4. Furthermore, as shown in Table 2.2, none of the listed methods is previously reported to be applicable for the RND-stacked graphene except for this work. The Si-peak analysis is extended in this work to include the RND-stacked graphene and various oxide thicknesses by studying the Si-peak model using both pristine and synthesized graphene. As later reported in Chapter 5, the Si-peak analysis is immune to most changes in the graphene quality because of the Si-peak produced at silicon far below graphene.

Table 2.2: Raman-based methods to determine the number of graphene layers. Notation below, $f(x)$ means spectral analysis, 'f' on 'x' peak(s). Stacking orders other than ABA are mentioned under the range if the method is also known to apply to such samples. Here LF and NA stand for low frequency and numerical aperture, respectively.

| **Method** | **Range** | **Pros** | **Cons** | **Experimental setups** | | | **Refs.** |
|---|---|---|---|---|---|---|---|
| | | | | **Laser (eV)** | **NA** | **Oxide (nm)** | |
| Ratio–$I(Si_G, Si_0)$ | 1–100 +ABC **+RND** | Relies on the main Si-peak. Insensitive to graphene. Discrete. | Needs reference, $I(Si_0)$ at bare substrate. Nonlinear model. | 2.33, 1.96 **2.33** | 0.45, 0.9, **0.95** | 89, **285**, **365** | [61, **this work**] |
| Ratio–$I(G, Si_G)$ | 1–100 +ABC | Linear relationship in loglog–plot. Discrete. | Oxide thickness and random stacking order sensitive. | 2.54, 2.33, 1.96 | 0.4, 0.45, 0.9 | 89, 104, 280, 300 | [46, 52, 56, 61, 101] |
| Ratio–I(2D, G) | 1–3 +ABC | Strong signal. | Oxide thickness and random stacking order sensitive. | 2.41, 2.33 | 0.6, 0.8 | 300 | [34, 46, 47, 52, 101] |
| Shape(LF–LBMs) | 1–20 | Sensitive to interlayer coupling. Absent in SLG. | Weak signal. May be blocked by notch filter. | 2.33, 1.96, 1.58 | | Suspended | [64] |
| Shape(N) | 1–8 +ABC | Absent in SLG. | Weak signal. Shadowed by the G-peak. | 2.81, 2.54, 2.41, 2.33, 1.96 | 0.8, 0.95 | 80, 100 | [29, 42, 43, 78] |
| Shape(M) | 1–8 +ABC | Absent in SLG. | Weak signal. | 2.81, 2.54, 2.41, 2.33, 1.96 | 0.8, 0.95 | 80, 100 | [17, 29, 42, 43, 66, 78] |
| Shape(CMs) | 1–5 | | Weak signal. | 2.81, 2.54, 2.41, 2.33, 1.96 | 0.8 | 100, 280, 300 | [17, 78, 86] |
| Shape(G*) | 1–5 +ABC | Good signal. | Very weak dependence. | 2.81, 2.54, 2.41, 2.33, 1.96 | 0.8 | 100 | [78] |
| Shape(2D) | 1–5 +ABC | Strong signal. | Irregular for random stacking. | 2.81, 2.54, 2.41, 2.33, 1.96 | 0.8 | 100, 300 | [18, 52, 65, 67, 78] |
| Pos(C) | 1–5 | Sensitive to interlayer coupling. Absent in SLG. | Noisy. Often notch filtered. Absent for ABC-stacking. | 2.33, 1.96, 1.58 | 0.9 | Suspended, 93, 300 | [29, 94, 96, 106] |
| Pos(G) | 1–4 | | Weak dependence. Stacking order sensitive. | 2.41, 2.33 | 0.8 | 100, 300 | [34, 36, 46, 52, 97] |
| Pos(2D) | 1–3 | | Weak dependence. Stacking order sensitive. | 2.33 | | 300 | [46, 52] |
| FWHM(2D) | 1–5 | | Very stacking order sensitive. | 2.33 | 0.95 | 285, 300 | [38, 46, 52] |
| I(Rayleigh) | 1–6 | Insensitive to graphene. | Noisy. Need expensive tool modifications. | 2.41, 1.96 | 0.95 | 300 | [8] |
| I(G) | 1–7 | | Oxide thickness and random stacking order sensitive. | 2.41, 2.33 | | 300 | [47, 52, 96, 101] |

# Chapter 3

# Experimental

## 3.1 Graphene Fabrication

There are various ways to fabricate SLG, BLG or N-LG and transfer them on to $SiO_2$/Si–substrate. As the main focus was also to study the physical grounds of Ratio–I($Si_G$, $Si_0$)–model, most samples were produced via mechanical exfoliation to ensure best possible quality of graphene. These samples consist of 285 nm or 365 nm thermal oxide. Moreover, few samples with random-stacked graphene on 365 nm $SiO_2$/Si–substrates were also fabricated using CVD of graphene, which is currently the best way to manufacture commercially viable large-area continuous monolayer graphene.

### 3.1.1 Mechanical Exfoliation of Graphene

Pristine graphene was obtained via mechanical exfoliation of Kish graphite using Scotch Magic 810-1933R –tape. Process steps shown in Figure 3.1a are as follows: 1) Two pieces of tape are taken, and one is operated by hand and another is attached adhesive-up to a solid surface. 2) Few pieces of graphite is put on the tape surface. 3) Tapes are pressed together and meticulously separated. This is repeated for ∼2 cm long area until the tapes begin to lose their adhesion as graphite/graphene pieces on tape begin to cover all of the adhesive. Such tape is ready for a transfer step.

Figure 3.1b shows the transfer of exfoliated graphene on bare ultrasonic cleaned $SiO_2$/Si–substrate in three steps: 1) Oxide surface first, substrate is pressed by hand to the graphite filled area on tape. 2) After few minutes, the sample is detached and analysed under a microscope. Most often only few if any SLG is found, making the whole process very low throughput. 3) The tape residuals are removed by cleaning the sample for 900 s and 60 s in acetone and isopropanol, respectively.

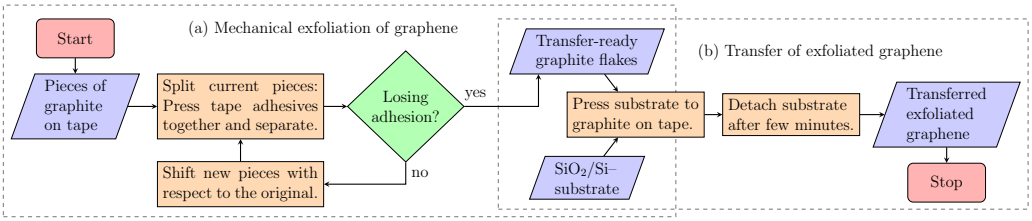


Figure 3.1: Flowchart on (a) mechanical exfoliation of graphene and (b) its transfer on to $SiO_2$/Si–substrate.

### 3.1.2 Chemical Vapour Deposition of Graphene

Large-scale artificially produced graphene can be fabricated on copper using a high throughput, high temperature CVD method. Although for this work CVD graphene samples were received as-transferred, they were fabricated, as illustrated in Figure 3.2a, as follows: 1) A chamber with a copper foil is heated up to 1000 $°C$, 2) Graphene nucleation sites on copper are formed and grown by introducing a methane-hydrogen gas mixture. 3) The chamber is cooled down in a controlled manner.

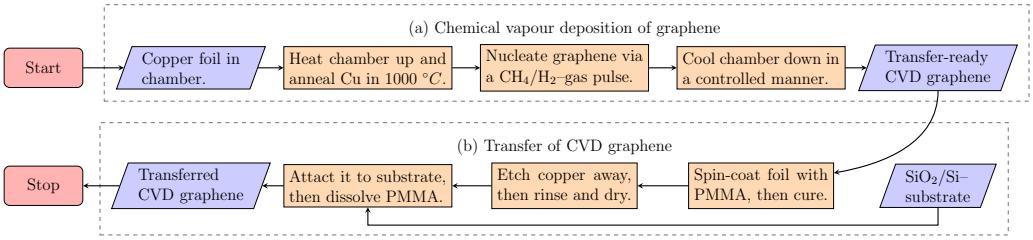


Figure 3.2: Flowchart on (a) CVD of graphene and (b) its transfer on to $SiO_2$/Si–substrate.

Researchers around the world have sought to achieve high quality reproducible single-crystalline monolayer growth of CVD graphene. The growth conditions are affected by many factors such as characteristics of the growth substrate, growth temperature, pressure, gas mixture ratio and cooling rate.

As shown in Figure 3.2b, graphene on copper foil was transferred on $SiO_2$/Si–substrate in three steps: 1) Foil with graphene is spin-coated with poly(methyl methacrylate) ($PMMA$) and it is thermally cured. 2) Copper is removed with an etchant, is rinsed and dried. 3) PMMA/graphene–sandwich is pressed on $SiO_2$/Si–substrate and PMMA is dissolved away with acetone.

## 3.2 Confocal Raman Spectroscopy

Raman microscopy is a spectroscopic characterization technique to detect Stokes (and anti-Stokes) Raman scattering for active molecular vibrational and rotational modes in the studied material. Energy-level diagram of Raman scattering is shown in Figure 3.3a. In this work, Raman spectrum of graphene was non-destructively measured using a confocal Raman spectroscope, WITec Alpha 300 RA, which was operated using 100× (NA 0.95) objective lens, 600 lines/mm grating, 532 nm laser excitation wavelength and 5.4 mW laser excitation power. Raman system is illustrated in Figure 3.3b–d.

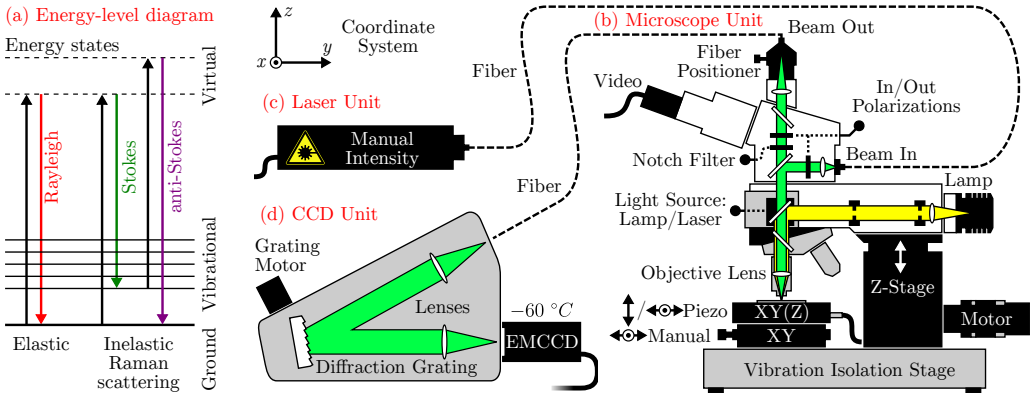


Figure 3.3: (a) Rayleigh, Stokes and anti-Stokes energy transitions at sample excitation. Scheme about WITec Alpha 300 RA Raman –system depicting (b) microscope, (c) laser and (d) CCD unit. Microscope utilizes confocal spectroscopy and Köhler illumination.

## 3.3 Tapping-Mode Atomic Force Microscopy

AFM is known for its low throughput but precise sample surface height topography imaging. Digital Instruments Dimension 3100 AFM –tool was used to verify the graphene thicknesses on $SiO_2$/Si-substrates. There are three AFM operation modes: (a) tapping, (b) contact and (c) non-contact. Their physical principles are demonstrated in Figure 3.4a–c. AFM of graphene was done in the tapping mode, in which the cantilever tip is in the intermittent contact with the sample. Tapping-mode AFM was chosen as it aims to combine the best properties of two others. It retains the contact mode resolution, while, due to minimal lateral forces, is less damaging to surface and more robust against imaging artefacts.

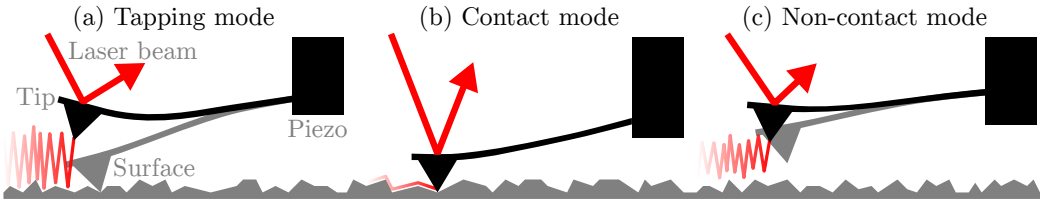


Figure 3.4: Working principle of (a) tapping, (b) contact and (c) non-contact AFM operation modes. Laser beam is deflected by a cantilever tip to a position sensitive photo-diode, converting a minuscule tip movement to a measurable change at the detector. Feedback to a piezoelectric stage permits a precise control of the distance between the tip and surface.

## 3.4 Single Wavelength Ellipsometry

Thin film thickness, uniformity and refractive index can be quickly obtained by single wavelength ellipsometry. Oxide thicknesses of $SiO_2$/Si–substrates were estimated using Philips Plasmos SD 2600 –tool, which determines the thin film features in four distinctive steps. First, a multilayer structure model is built using user given thicknesses and refractive indices. All model parameters, except for the film of interest, are fixed. Second, a single wavelength laser beam, with known angle of incidence, intensity, linear polarization and wavelength, is directed at a sample, where the beam changes its polarization to elliptic at the reflection. Then, the reflected beam goes through a rotating polarizing filter and its amplitude ratio, $\Psi$ and phase difference, $\Delta$ are measured by a photo-diode. Third, the model is numerically fit to the observed data to determine thickness and refractive index of the film. Finally, the mean and standard deviation of the film parameters are calculated.

## 3.5 Scanning Electron Microscopy

In contrary to optical imaging, SEM uses a focused beam of electrons to produce high resolution large area scan images of a sample. These electrons are accelerated to energies of 0.1–100 keV and precisely focused at the sample by a carefully designed system of coils. At the sample various signatures are generated: secondary, backscattered and Auger electrons, and X-ray and visible spectrum photons. Energetic electrons allow high resolution imaging beyond diffraction limit. However, the more acceleration voltage and zoom level are increased, the more destructive SEM imaging becomes. Field emission SEM Carl Zeiss Supra 40 –tool was operated at low acceleration voltage to image CVD graphene layers.

# Chapter 4

# Model

This chapter introduces the details of the Si-peak intensity model used in this work. The model allows accurate wide-range estimation of the number of graphene layers on $SiO_2$/Si–substrates using the Raman measured Si-peak intensity data, also denoted as Ratio–I($Si_G$, $Si_0$) or I($Si_G$)/I($Si_0$). Its conceptual presentation is given in Section 4.1. The essential data pre-processing steps are described in their corresponding subsections in Section 4.2. The model itself is introduced in Section 4.3. Processing steps of the model are depicted in Section 4.4 using FLG as a process flow example. Theoretical grounds of the model are presented in Section 4.5, where the underlying assumptions are described and the equations rigorously derived. Cross-correlation of the model output with a constructed FLG thickness reference and an AFM scan data is discussed in Section 4.6.

## 4.1 Conceptual Presentation of Model

This section gives a general view of the model used in this work. The main process flow, including where they are found in this thesis, is shown in Figure 4.1, beginning from the Raman measurements, and ending with the results. First step is to process the measured Raman scan maps, obtained from multiple samples, in order to combine them together. Second, the number of graphene layers is estimated using the corrected and normalized Si-peak intensity maps. Third, the thickness verification maps are constructed via alternative sources such as AFM and Raman 2D-peak. Fourth, the estimated graphene thickness map is compared to the verification and AFM maps, and correlated with other Raman maps, such as the 2D-peak position. Finally, the results are presented and the findings discussed.

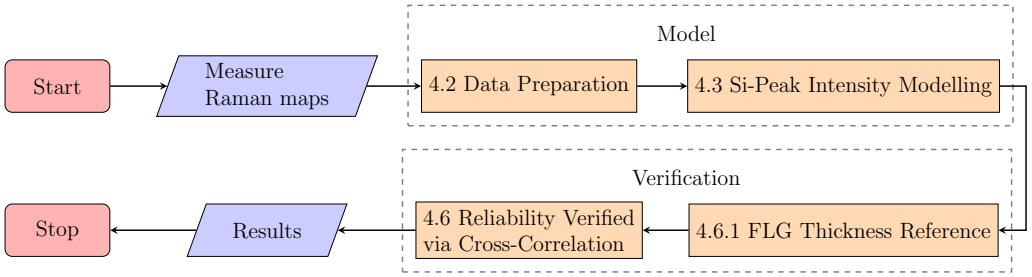


Figure 4.1: Flowchart of the conceptual presentation of the model. Each process node represents a section found in this chapter. Output node represents a chapter containing the results analysis.

## 4.2 Data Preparation

The data can be distorted to some degree by unintentional differences between and during the measurements due to changes in the laboratory environment and measurement setup. These differences are relevant factors when analysing multiple datasets and typically require some data preparation steps before the datasets can truly be combined. In this work, three significant factors were accounted for: 1) fluctuations in the intensity and wavelength of the Raman laser, 2) drift in the sample height position of the Raman microscope, and 3) variation in the sample tilt angle. A great caution was taken to avoid complex, or otherwise non-physical, data preparation steps. Each step, is summarized in Figure 4.2, which gives a general process flow of the data preparation.

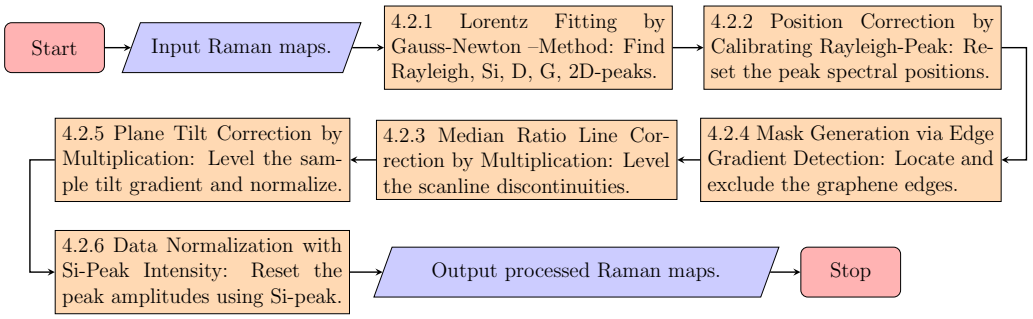


Figure 4.2: Flowchart of Raman scan data preparation. Each node, summarizing a subsection, represents a process step found in this section.

### 4.2.1 Lorentz Fitting by Gauss-Newton –Method

Lorentzian lineshape is a common spectral feature in Raman spectroscopy of graphene due to the homogeneous broadening of spectral lines, and is used through-out this work. A need for computer-assisted analysis emerged when an extensive correlation study, between various Raman-based layer-number fingerprints, was planned. After a careful matrix-based derivation and sparse-matrix implementation, it finally could simultaneously fit Lorentzians to over two thousand Raman spectra per second. In terms of the Si-peak analysis, this step is not required, because full width at half maximum of the Si-peak is fairly constant regardless the number of layers. In other words, there is nearly no distinction between normalized area and intensity maps for Si-peak. Nevertheless, the fitting is also carried out for the Si-peak to access the intensity map, to minimize errors.

For the lineshape fitting prodecure, it was decided to utilize a simple and robust iterative minimization algorithm, Gauss-Newton –method. It is obtained from a common Taylor-series first-order –approximation, Newton-Raphson –method by ignoring the second-order derivative terms. To clarify, the time consuming evaluation of the Hessian matrix is avoided. It was observed that, for Lorentzian lineshape, Gauss-Newton –method is less sensitive to uncertainty in initial guess than its predecessor, making it more robust against noise. Such conditions are common in non-Si-peak analysis, therefore justifying the decision to use it, albeit the loss of guaranteed quadratic rate of convergence. Nevertheless, a solid initial guess is still required for convergence and is found by algorithmically estimating the amplitude, centre, FWHM, and offset of the peak by separating the Lorentzian signal from linear background.

### 4.2.2 Position Correction by Calibrating Rayleigh-Peak

To restore the ability to combine the data for peak positions obtained for multiple samples, their Rayleigh-peaks must be calibrated to zero for each sample individually. Utilizing the Lorentzian-to-spectrum –fitting introduced in Section 4.2.1, the Rayleigh-peak position Raman shifts can be reset to zeros within the spectral resolution. Relation for Raman shift, $\Delta k = (\frac{1}{\lambda_0} - \frac{1}{\lambda_1})$ can be used to prove that this calibration step automatically and correctly places all other spectral positions. It was calculated that $\pm 0.1$ nm fluctuations in the excitation wavelength are enough to produce $\mp 3.5$ cm$^{-1}$ Raman shifts. Similar Rayleigh-peak displacement was observed in this work and it could be explained by thermal fluctuations in the Raman laser unit.

### 4.2.3 Median Ratio Line Correction by Multiplication

To level the scanline discontinuities found in the raw Raman measurement data, a numerical algorithm was designed for this work. Median Ratio Line Correction by Multiplication (*MRLCM*) was developed to safely, keeping the essential intensity ratios untouched, correct the horizontally distorted measurement data obtained from the Raman tool. The measurements are affected by three possible types of scanning distortions: 1) discontinuities between horizontal scanlines, 2) a gradient due to the sample tilt, 3) scars along the scanning lines. Vast majority of the data was plagued only with the first type, which MRLCM can fully correct without issues. The second type can only be horizontally corrected because the gradient has both vertical and horizontal components. However, the third type cannot be corrected by MRLCM but fortunately the scarring was found to be extremely rare.

Principle of MRLCM is simple as shown in Figure 4.3: i) A distorted intensity map, $I$ and an optional inclusion mask, $M$ are taken as input. ii) A filtered ratio map, $R$ is created by calculating ratios between the consecutive horizontal lines. For the first line, which has no line above it, the ratios are set to one. Also, if either of the two corresponding mask values for each given intensity map element is true, then the ratios will be set to special Not-a-Number ($NaN$) value, what will later be ignored. iii) A median value, $m_i$ is calculated for each line of the filtered ratio map, $R_{i,1:m}$. NaN values are treated as missing data and ignored. If the given line has only NaN values, then the median ratio will be one. iv) A cumulative product of medians, $c$, is evaluated starting from the first reference line and progressing towards the last line. In other words, the first line is completely unaffected by MRLCM. v) The intensity map discontinuities are levelled by multiplying each line, $I_{i,1:m}$ by the corresponding cumulative product value, $c_i$. vi) The corrected intensity map, $I$ is given as output.

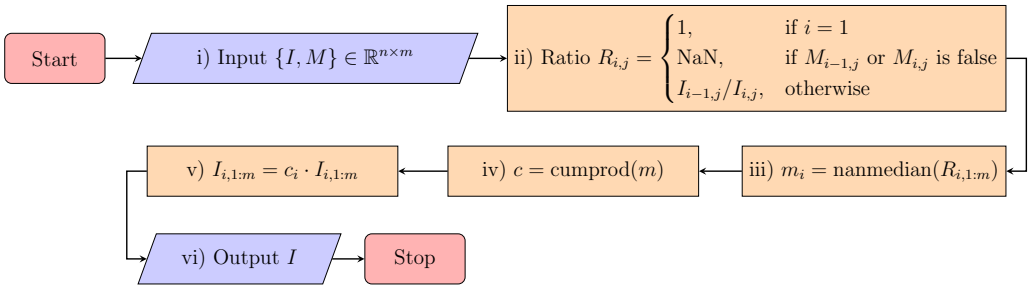


Figure 4.3: Flowchart of the MRLCM–algorithm using matrices. Figure 4.7 in Section 4.4 depicts the procedure with a practical FLG example.

The main advantage of MRLCM over many other line correction algo-

rithms is that this preserves the essential intensity ratios, which are needed to determine the number of graphene layers. In other words, the data remains physical. Additionally, MRLCM is fairly robust against outliers because the median is a statistically robust measurement of central tendency. While, in theory, the median performance would degrade for an extremely noisy data, in practice, the Raman tool produces strong Si-peak signals with low noise. Only real downside is that sometimes the algorithm is offset by physical features, such as graphene edges. Fortunately, the Si-peak analysis is fairly insensitive to such features, but other Raman peaks needed for correlation study, such as G and 2D, produce huge gradients at the graphene edges. MRLCM performance may be further improved by guiding the algorithm using a mask, $M$, which is used to exclude the unwanted graphene edges and other physical features that result in intensity gradient. Next section describes an automated generation of such an inclusion mask, which will further improve the levelling accuracy.

### 4.2.4 Mask Generation via Edge Gradient Detection

While not essential for the Si-peak analysis, other Raman analyses, suffering from major intensity gradients, require an inclusion mask to guide MRLCM in order to produce reliable leveling. To solve this problem, a mask generation algorithm, based on the detection of the vertical components of gradients, was developed. It was found that the intensity ratios along vertical lines were completely immune to the scanline discontinuities, a problem MRLCM tries to solve, while they remained sensitive to the edge features. Such a vertical ratio map was used to detect the vast majority of unwanted gradients and to construct a needed inclusion mask. Furthermore, the sensitivity to gradients was found to intensify by taking a geometric mean of two or more consecutive vertical lines. Reasoning behind this relies on the fact that neighbouring pixels correlate, if physical dimensions of the pixel are less than the diffraction limit, and geometric mean combines the correlating information. This work uses two vertical lines to preserve simplicity.

Principle can be summarized as follows: 1) A geometric mean of two or more ratios is taken along the consecutive vertical lines. 2) All negative, zero and infinite ratios are treated as invalid, and set to NaN value. Also, the user given mask is honoured, and the excluded pixels are set to NaN value. 3) The ratio map is transformed to log–space in order to calculate a geometric mean. 4) Clever mean and variance [5] of the log–ratios are evaluated. This algorithm takes care of the possible outliers, and treats NaN values as missing data. 5) A mask is generated by treating all log–ratios farther than two sigmas away from the calculated geometric mean as features to exclude.

### 4.2.5 Plane Tilt Correction by Multiplication

As discussed in previous Section 4.2.3, the Raman measurement can also be distorted by the sample tilt angle during the scan, what is seen as a sample-wide gradient. Horizontal part of the gradient remains after MRLCM–algorithm, and may affect the Si-peak analysis, or Ratio–I($Si_G$, $Si_0$), which relies on the intensity ratio between the Si-peak measured at graphene, I($Si_G$) and at substrate, I($Si_0$). Moreover, offsets were found to exist between the peak intensity depth profiles along the laser beam axis, as shown in Figure A.1, and are hypothesized to result from the differences in unique interference patterns for each peak. This would explain why Plane Tilt Correction by Multiplication ($PTCM$) seems to distort the correlation between Si-peak and other different Raman peaks, such as G and 2D, even if the PTCM results are levelled. While this gives an understanding on what physically happens during the distortions, it was not further studied in this work.

For simplicity, a simple plane fit to substrate, I($Si_0$) is performed. A mask is used to mark the substrate area. Then the intensity map is multiplied by the inverse of the fitting result. In effect, this normalizes the map, which is useful in the Si-peak analysis. This can be further developed by implementing physically realistic models such as 2D Lorentzians.

### 4.2.6 Data Normalization with Si-Peak Intensity

Raman peaks such as 2D and G were normalized with respect to averaged substrate Si-peak, I($Si_0$) per measurement. This subsection discusses two complications that arose during the attempt to cross-correlate peak-to-peak ratios using normalized data. A possible workaround is also presented.

When a number of samples accumulated, it was found that peak-per-peak amplitude ratios varied from sample to sample, even if the intensity adjustment setting was set identical during Raman measurement. Although the Si-peak analysis itself is not affected by this issue, the peak-to-peak information such as Ratio–I(2D, G) and Ratio–I(G, $Si_G$) vary and introduce difficulties in combining data for cross-correlation analysis. It occurs even though it was a routine procedure to wait several minutes for the CCD unit to cool down and the laser unit to thermally stabilize before the actual measurements. Rather, it is believed to be caused by the offsets in Raman peak intensity depth profiles, introduced in previous Section 4.2.5 and shown in Figure A.1. Consequently, the offsets affect Raman spectral shape based on which Raman peak the beam was chosen to be focused at before each measurement. The beam was focused at the Si-peak for most but not all samples in this work, which sheds light on the problem root. This problem is seen as

inconsistencies in combined datasets.

Furthermore, Si-peak amplitude maps that were distorted by focal point drift in depth-direction described in Section 4.2.3 and corrected by MRLCM–algorithm, are likely to face the same problem. While MRLCM successfully restores the amplitude map flatness, it does not know the exact movement of focal point in depth-direction, which causes the imbalance in peak ratios as shown in Figure A.1.

Normally MRLCM–algorithm sets the first scanline as a reference. A possible workaround is to 1) locate the scanline where the average Si-peak intensity maximizes, focusing the beam at the Si-peak, and 2) for each peak, operate MRLCM–algorithm using the located scanline as a reference line. This procedure ideally restores peak-to-peak ratios to that of the ratios when beam is focused at the Si-peak, and allows them to be combined for cross-correlation study. However, it is not done in this work, because non-Si-peak maps are limited to graphene boundaries and do not always contain the reference scanline within their scope.

## 4.3 Si-Peak Intensity Modelling

Four general aspects of the Si-peak modelling are discussed in this section: 1) The summary of theoretical background for the calculating model, 2) The determination of the number of graphene layers from the measured Si-peak intensities via linear comparison with the calculated Si-peak intensities, 3) The research and reasoning behind the choice for the graphene anisotropic complex refractive indices, and 4) The sensitivity of the model to uncertainty in the key input parameters.

### 4.3.1 Summary of Model Theoretical Background

The model uses a multilayer structure, where the top and bottom layers are semi-infinite in nature, and each medium can be uniaxial anisotropic. In this work, the layers from top to bottom are air, graphene, silicon oxide, and silicon. The light propagation is calculated in two main steps: 1) Propagation of incoming light, through the multilayer structure, in to the substrate, where it produces Raman scattering, or the Si-peak intensity, and 2) Propagation of scattered light out of the multilayer. Each step has its own wavelength and cannot interfere with each other. All possible internal reflections are accounted for using a recursive effective reflection coefficient –formula to, one-by-one, replace all the finite layers with an effective semi-infinite layer, working from the last to the first. The result is equivalent to that of the ma-

trix formalism. Anisotropic Fresnel reflection and transmission coefficients with the anisotropic propagation modes form the very core of this model. They are derived in Section 4.5. To further increase the model accuracy, the Raman laser beam propagation is approximated with a multi-ray model. The beam is assumed to be a linearly polarized TEM00-mode Gaussian beam, which is focused through a lens objective with a well-defined numerical aperture. The beam is assumed to enter the lens in normal incidence, and be well confined within the lens diameter. Finally, the total intensity is calculated by integrating over the rays.

### 4.3.2 Determining the Number of Graphene Layers

The principle of determining the graphene thickness from the Si-peak intensity is based on linear interpolation and is summarized in Figure 4.4. First, a normalized Si-peak intensity map with meta data is taken as input. The meta data includes silicon oxide thickness, excitation wavelength, peak spectral position, numerical aperture and anisotropic complex refractive indices for each layer in the structure for both absorption and scattering wavelengths. Second, the theoretical model, described in Section 4.5, is used to calculate the Si-peak intensity for a wide range of graphene thicknesses. Third, the number of graphene layers is interpolated for each pixel by doing a linear comparison between the measured and calculated intensities. Finally, the generated number of layers map is given as output.

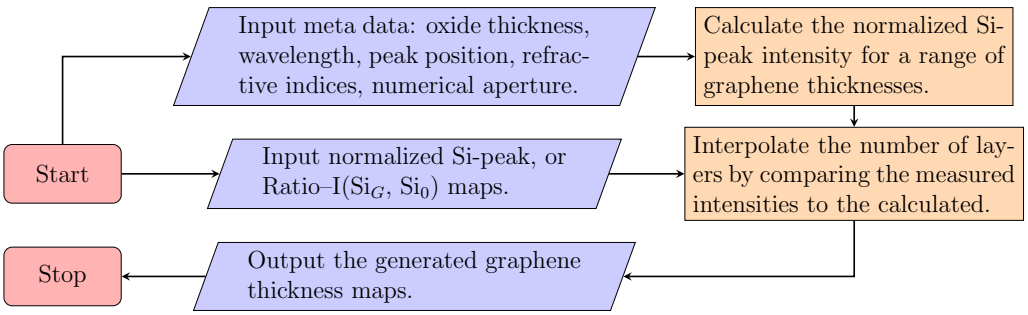


Figure 4.4: Flowchart of determining the graphene thickness by the Si-peak intensity modelling.

### 4.3.3 Selecting the Graphene Refractive Indices

As the graphene anisotropic complex refractive indices are one of the key factors in the model, using physical and consistent indices is extremely im-

portant in terms of model accuracy and reliability. However, obtaining a reliable and widely accepted anisotropic complex refractive indices for graphene is challenging. Due to its unusual two-dimensional nature, the current tools for determining its optical properties are nearing their limits, and produce results that are sensitive to non-ideal phenomena, such as moisture, contaminants, surface roughness, coupling with the substrate, and other dynamic effects [68, 81].

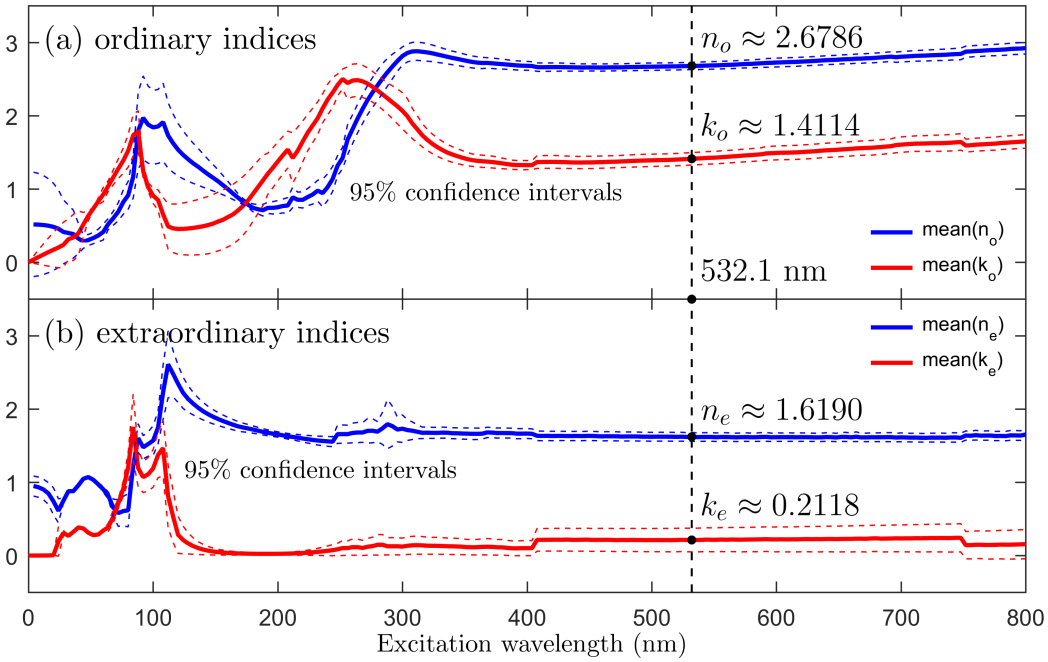


Figure 4.5: Averaged real and imaginary parts of the graphene complex refractive indices, $\tilde{n}_{g,o}$ and $\tilde{n}_{g,e}$ with 95 % confidence intervals for (a) ordinary and (b) extraordinary waves. Datasets begin or end at the discontinuities.

To ensure a wide perspective on graphene optical properties, in total 13 studies were analysed and 27 datasets digitized. This number includes 10 datasets, which were obtained from 2 different ab-initio calculations. Therefore, 17 datasets for in-plane ordinary indices and 10 for out-of-plane extraordinary indices were collected, both required for uniaxial anisotropic graphene model. As evident in Figure A.2, the datasets from different sources are somewhat conflicting with each other. The inconsistency is more significant for the extraordinary case, in which the measurement uncertainty is higher because the out-of-plane dimension of graphene is vanishingly thin. It was decided to use a weighted arithmetic mean of all found datasets, where each article has a total weight of one, divided to all its datasets. The averaged

ordinary and extraordinary indices, $\tilde{n}_{g,o}$ and $\tilde{n}_{g,e}$ for visible spectrum range are shown in Figure 4.5. It was found that the indices are fairly constant in visible range, meaning that they are insensitive to possible wavelength fluctuations for incident and scattering light. This is good for this work as the Raman laser excitation wavelength is 532 nm.

### 4.3.4 Sensitivity to Uncertainty in Model Parameters

In previous subsection, it was demonstrated that there is a degree of uncertainty in the graphene refractive indices, which, to date, has not been resolved yet. This subsection aims to provide insight on how would the model be affected by such deviations. There are three input parameters, which have a significant uncertainty: a) graphene refractive indices, b) oxide thickness of the substrate, and c) numerical aperture ($NA$). There exists uncertainty in many other parameters such as excitation wavelength, graphene thickness and other refractive indices, but these were found to be insignificant. The model sensitivity to these uncertainties were tested in two ways: 1) Each input parameter with significant uncertainty was varied by $\pm 5$ %, while keeping others constant, as is shown in Figure 4.6a–c. 2) Such parameters were varied by $\pm 1$ % in all possible combinations, as is shown in Figure 4.6d. Two different oxide thicknesses, 285 nm and 365 nm were used as a model testbed in this work. 285 nm oxide thickness is located at an optimal contrast region for graphene visibility, whereas 365 nm is near the worst.

Figure 4.6a shows the model sensitivity to variation in the graphene complex refractive indices, $\tilde{n}_{g,o}$ and $\tilde{n}_{g,e}$ for incident and scattering wavelengths. It is found that $\pm 5$ % uncertainty produces similar deviation for both oxide thicknesses. For FLG, the deviation stays less than one layer and is acceptable. However, for thicker graphene samples, the layer counting error becomes a relevant factor. Therefore, more research is needed to narrow down the uncertainty on graphene refractive indices. A possible workaround towards greater model accuracy can be achieved via exhaustive numerical fitting to observations, but it is not within the scope of this work.

Likewise, model sensitivity to the oxide thickness uncertainty is evaluated due to possible systematic error in oxide thickness ellipsometry measurements. Figure 4.6b reveals that samples with 365 nm oxide are significantly affected by oxide thickness uncertainty, while those with 285 nm oxide are nearly immune to it. Explanation is that the local derivative of the Si-peak intensity is zero near 285 nm, while at maximum near 365 nm, as is experimentally demonstrated by Figure 5.4a in Chapter 5. In other words, the sensitivity can avoided by either choosing an oxide thickness in one of the zero derivative regimes, or by determining the oxide thickness with a precise

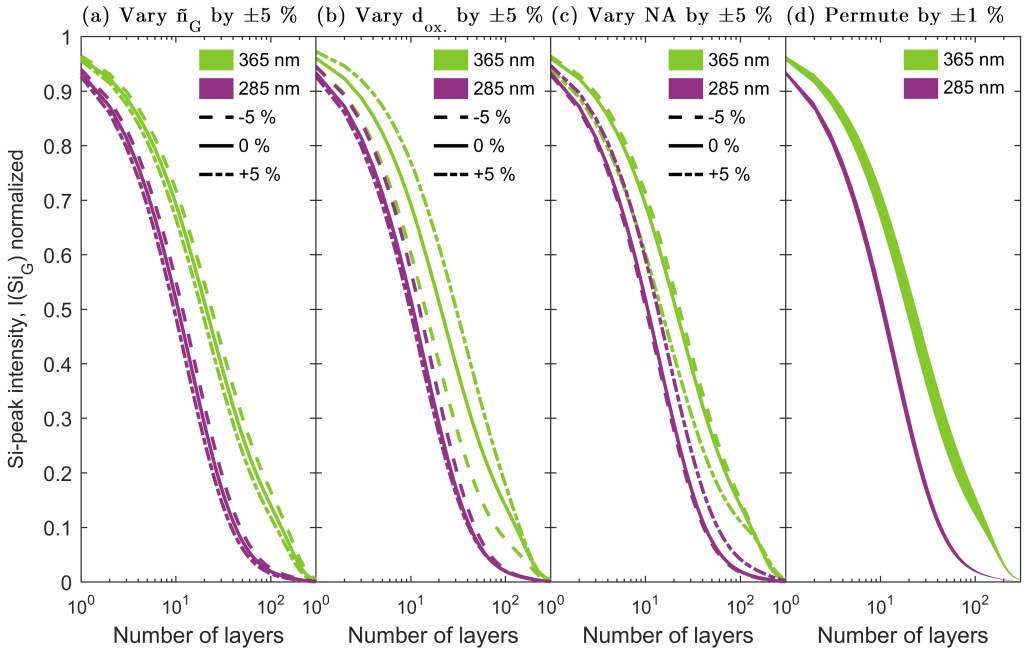


Figure 4.6: Model sensitivity to uncertainty using manufacturer specified NA and excitation: 0.95 and 532 nm. Tests were carried out for 285 nm and 365 nm oxide thicknesses. Model parameters, (a) graphene complex refractive indices, (b) silicon oxide thickness and (c) numerical aperture, were varied by ±5 %. Panel (d) shows the permuted ±1 % variation of the parameters.

and accurate tool such as spectroscopic ellipsometer or profilometer.

Numerical aperture was also tested because, despite knowing a manufacturer specified objective lens NA, the exact beam confinement, or how many beam waists fits through the lens, remains uncertain and is dependent on the confocal microscope design. The beam confinement and its relationship to NA is further discussed in Section 4.5.1. Although it is unlikely that NA would be higher than that of the manufacturer specified, its effect is also shown in Figure 4.6c. Excluding the unlikely higher NA, both oxide thickness regimes are nearly immune to the NA uncertainty.

Figure 4.6d demonstrates an overall model sensitivity to combined uncertainty in these three major parameters if varied by ±1 % together. It can also be interpreted as an overall model prediction uncertainty per oxide thickness, when all model parameter uncertainties are narrowed together down to within 1 % variance. It is found that the model for 365 nm oxide thickness has about twice as large tendency for layer counting errors than that of 285 nm. Taking into account the possible few percentage errors in AFM [91] or ellipsometry, the shown results are considered acceptable.

## 4.4 Process Explained in Pictures

Two previous sections discussed the model process steps, which are represented below in Figure 4.7 with a practical Si-peak analysis example done step-by-step for a FLG flake. It demonstrates the great agreement between the reference thickness map and that of calculated, and the vast significance of MRLCM–algorithm, which preserves the delicate $I(Si_G)/I(Si_0)$ ratios.

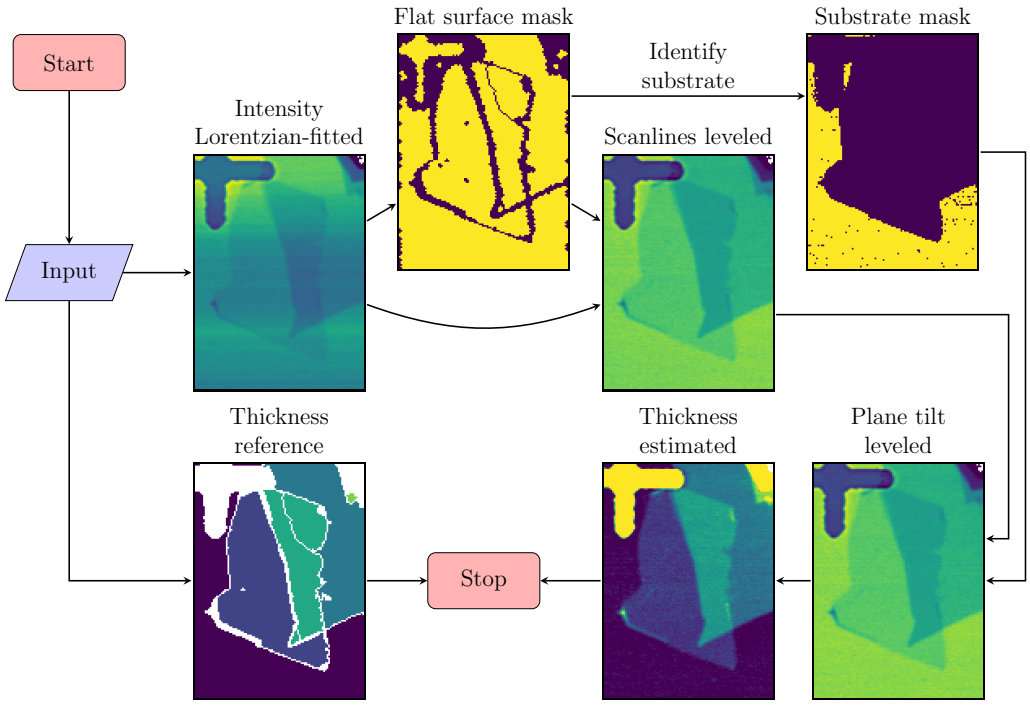


Figure 4.7: Flowchart of the Si-peak analysis depicted using a FLG example. Detailed explanation of the scanline levelling by MRLCM–algorithm is given in Figure 4.2. The graphene thickness estimation is described in Figure 4.4.

## 4.5 Numerical Model via Physical Theory

The number of graphene layers can be determined using the spectral information on an absorbed silicon signal through graphene, $I(Si_G)$ and that of the bare substrate, $I(Si_0)$. Raman spectra of few-layer graphene and the silicon underneath is obtained with confocal Raman microscopy. Measured relative change in the Si-peak intensity, Ratio–$I(Si_G, Si_0)$ is modelled in order to determine the number of graphene layers. Two main focuses in this section are

theoretical simplifications and model derivation. Their process flows leading to the numerical model are summarized in Figure 4.8.

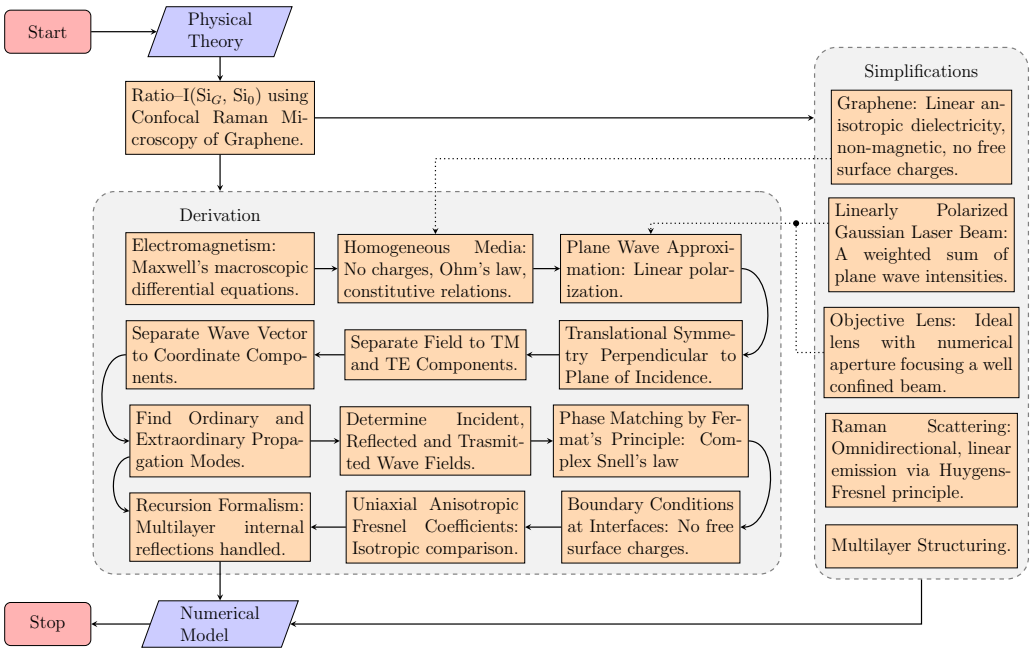


Figure 4.8: Flowchart of theory simplifications and model derivation.

### 4.5.1 Simplifications

This section discusses the five key theoretical simplifications, shown in Figure 4.8, on the following aspects: 1) graphene material properties, 2) laser beam characteristics and propagation, 3) objective lens beam confinement and focusing, 4) Raman scattering and the Si-peak emission, and 5) sample multilayer structure and interfaces.

Graphene was optically most complicated medium of the multilayer structure for this work. Therefore, its model will define limits on how far the initial differential equations can be simplified. However, an accurate optical model is required because graphene is an essential part of the model. Due to an extensive evidence presented in Section 4.3.3, graphene is assumed to be an azimuthally symmetric uniaxial anisotropic medium, which has two complex refractive indices, $\tilde{n}_{g,o}$ and $\tilde{n}_{g,e}$ for ordinary in-plane and extraordinary out-of-plane propagation modes. These optical parameters are assumed to be homogeneously distributed within graphene dimensions and insensitive to the number of graphene layers. Furthermore, graphene is treated as a

non-magnetic, $\mu_g \approx \mu_0$, perfectly flat crystal with a constant thickness of 0.335 nm [3, 92] and zero free surface charges, $\rho_f$.

The confocal Raman microscope utilizes a focused linearly polarized solid-state laser beam to measure graphene Raman spectrum. Even if the beam was assumed to be a perfect linearly p-polarized TEM00-mode Gaussian beam, its non-linear nature would require computationally expensive finite element method, or similar kind, to find a solution to the problem. Such a beam is radially Gaussian distributed, diverges over distance and exhibits a well known non-linear Gouy phase shift near the focal plane. It was decided that the beam is approximated with a weighted sum of rays, where each ray has its own intensity and angle of incidence based on the underlying distribution. Furthermore, each ray, due to mathematical equivalence, can be treated as a plane wave. This is the key simplification in order to find the anisotropic propagation modes and Fresnel coefficients per ray.

High-grade objective lenses, such as those used in modern confocal microscopes, are well characterized by their dimensionless numerical aperture value, $\mathrm{NA} = n_1 \sin\theta_1$, which determines the maximum angle for Snell's law operating on the lens. The $100\times$ objective lens with $\mathrm{NA} = 0.95$ used in this work is approximated as a perfect ideal lens. Furthermore, because of the Gaussian distribution nature, the beam truncation in lens must be considered. The beam is believed to be well confined and fit in three beam waists, $3w_0$, to obtain a balance between the beam distortion and the spatial resolution. However, the beam truncation factor is likely to vary with the tool, and should be experimentally measured. Another consequence of the lens approximation is that the p-polarization averages out and the rays focused at sample are approximately random polarized.

When the incoming light propagates through the multilayer structure and enters the substrate, it begins to excite the silicon atoms, which, in turn, vibrate and produce the Si-peak Raman emission. For simplicity, the Raman scattering intensity is assumed to be linearly proportional to that of the incident light, and its radiation profile to be omnidirectional, where each atom acts as a spherical wave source. Utilizing a well known Huygens-Fresnel principle, it can be deduced that the incident plane wave, exciting a plane of silicon atoms, would produce a reflected plane wave with its corresponding Raman emission wavelength. Therefore, Raman scattering is emulated with a perfect mirror, which shifts the wavelength. These scattered waves are assumed to be perfectly collected by the lens and directed to CCD–unit.

Each sample is considered to be of a multilayer sandwich, where each layer is homogeneous and has a well known invariant thickness and optical parameters. In other words, the model assumes that there exists no surface roughness, moisture, contaminants, defects, free surface charges or distor-

tions of any kind. The structure used in this work consists of air, graphene, silicon oxide and silicon. The first and last layers are assumed semi-infinite, where a portion of light escapes. All the infinite internal reflections are accounted for via recursion formalism.

### 4.5.2 Derivation

Focused beam of light is made of electromagnetic fields, which obey general time harmonic macroscopic Maxwell's differential Equations 4.1–4.1. Here $\boldsymbol{E}$ is electric field, $\boldsymbol{H}$ is magnetic field strength, $\boldsymbol{B}$ is magnetic flux density, $\boldsymbol{D}$ is electric displacement field, $\boldsymbol{J}$ is free current density, $\omega$ is field angular frequency and $\rho$ is medium charge density. In time harmonic form, all time varying field quantities, $\tilde{\boldsymbol{F}}$ are expressed in phasor form, $\boldsymbol{F} = \mathrm{Re}\left\{\tilde{\boldsymbol{F}} e^{-i\omega t}\right\}$, where $\boldsymbol{F}$ is a complex field in frequency domain. In other words, simplification, $\frac{\partial}{\partial t} \to -i\omega$ is permitted by the Fourier theorem.

$$\boldsymbol{\nabla} \times \boldsymbol{E} = i\omega \boldsymbol{B}, \qquad \text{The Maxwell–Faraday equation} \tag{4.1}$$

$$\boldsymbol{\nabla} \times \boldsymbol{H} = \boldsymbol{J} - i\omega \boldsymbol{D}, \qquad \text{The Maxwell–Ampère equation} \tag{4.2}$$

$$\boldsymbol{\nabla} \cdot \boldsymbol{D} = \rho, \qquad \text{Gauss' law} \tag{4.3}$$

$$\boldsymbol{\nabla} \cdot \boldsymbol{B} = 0, \qquad \text{Gauss' law for magnetism} \tag{4.4}$$

#### Homogeneous Media

Few material specific assumptions are made to simplify the Maxwell equations. All materials are assumed to be anisotropic, homogeneous, free from charge, $\rho \approx 0$ and non-magnetic, $\boldsymbol{M} \approx 0$. Therefore, the constitutive relations become $\boldsymbol{B} = \mu_0 \boldsymbol{H} + \boldsymbol{M} \approx \mu_0 \boldsymbol{H}$ and $\boldsymbol{D} = \epsilon_0 \boldsymbol{E} + \boldsymbol{P} = \epsilon_0 \overline{\overline{\epsilon}}_D \boldsymbol{E}$, and Ohm's law, $\boldsymbol{J} = \overline{\overline{\sigma}} \boldsymbol{E}$. They are utilized to simplify Equations 4.1–4.4.

$$\boldsymbol{\nabla} \times \boldsymbol{E} = i\omega \boldsymbol{B}, \tag{4.5}$$

$$\boldsymbol{\nabla} \times \boldsymbol{B} = \mu_0 \overline{\overline{\sigma}} \boldsymbol{E} - i\omega \mu_0 \epsilon_0 \overline{\overline{\epsilon}}_D \boldsymbol{E}, \tag{4.6}$$

$$\boldsymbol{\nabla} \cdot (\epsilon_0 \overline{\overline{\epsilon}}_D \boldsymbol{E}) = 0, \tag{4.7}$$

$$\boldsymbol{\nabla} \cdot \boldsymbol{B} = 0, \tag{4.8}$$

Using a well known relation for speed of light, $\mu_0 \epsilon_0 = 1/c_0^2$, Equation 4.6 can be written as $\boldsymbol{\nabla} \times \boldsymbol{B} = (\frac{\overline{\overline{\sigma}}}{\epsilon_0} - i\omega \overline{\overline{\epsilon}}_D) \boldsymbol{E}/c_0^2$. Furthermore, the right-hand side, can be written as $-i\omega \overline{\overline{\epsilon}} \boldsymbol{E}/c_0^2$, where $\overline{\overline{\epsilon}} = \overline{\overline{\epsilon}}_D + i\frac{\overline{\overline{\sigma}}}{\omega \epsilon_0}$ is the relative dielectric permittivity tensor. Taking a divergence of both sides provides a way to

simplify Equation 4.7 as $\boldsymbol{\nabla} \cdot (\epsilon_0 \bar{\bar{\epsilon}}_D \boldsymbol{E}) = \boldsymbol{\nabla} \cdot (\epsilon_0 \bar{\bar{\epsilon}} \boldsymbol{E}) = 0$.

$$\boldsymbol{\nabla} \times \boldsymbol{E} = i\omega \boldsymbol{B}, \tag{4.9}$$

$$\boldsymbol{\nabla} \times \boldsymbol{B} = -i\frac{\omega}{c_0^2} \bar{\bar{\epsilon}} \boldsymbol{E}, \tag{4.10}$$

$$\boldsymbol{\nabla} \cdot (\epsilon_0 \bar{\bar{\epsilon}} \boldsymbol{E}) = 0, \tag{4.11}$$

$$\boldsymbol{\nabla} \cdot \boldsymbol{B} = 0, \tag{4.12}$$

As discussed in Section 4.5.1, graphene is modelled as an azimuthally symmetric uniaxial anisotropic material, for which the relative dielectric permittivity tensor is diagonal and has symmetric in-plane x- and y-components. Out-of-plane z-component is called the extraordinary mode. The tensor can then be written as:

$$\bar{\bar{\epsilon}} = \begin{bmatrix} \epsilon_o & & \\ & \epsilon_o & \\ & & \epsilon_e \end{bmatrix} \tag{4.13}$$

By separating vectors and tensors into their coordinate components, Equations 4.9 and 4.10 can be expressed as six coupled differential equations:

$$\frac{\partial E_z}{\partial y} - \frac{\partial E_y}{\partial z} = i\omega B_x \qquad \frac{\partial B_z}{\partial y} - \frac{\partial B_y}{\partial z} = -i\frac{\omega}{c_0^2}\epsilon_o E_x \tag{4.14}$$

$$\frac{\partial E_x}{\partial z} - \frac{\partial E_z}{\partial x} = i\omega B_y \qquad \frac{\partial B_x}{\partial z} - \frac{\partial B_z}{\partial x} = -i\frac{\omega}{c_0^2}\epsilon_o E_y \tag{4.15}$$

$$\frac{\partial E_y}{\partial x} - \frac{\partial E_x}{\partial y} = i\omega B_z \qquad \frac{\partial B_y}{\partial x} - \frac{\partial B_x}{\partial y} = -i\frac{\omega}{c_0^2}\epsilon_e E_z \tag{4.16}$$

### Plane Wave Approximation

As explained in Section 4.5.1, the focused laser beam, even in its simplest form, is non-linear. To find an analytical solution, the beam is approximated with a weighted sum of plane waves. Each wave has its own amplitude, angle of incidence and polarization. The laboratory coordinate system, shown in Figure 4.9, is chosen so that xz-plane is the plane of incidence and z-coordinate is parallel with the surface normal. As a consequence, this

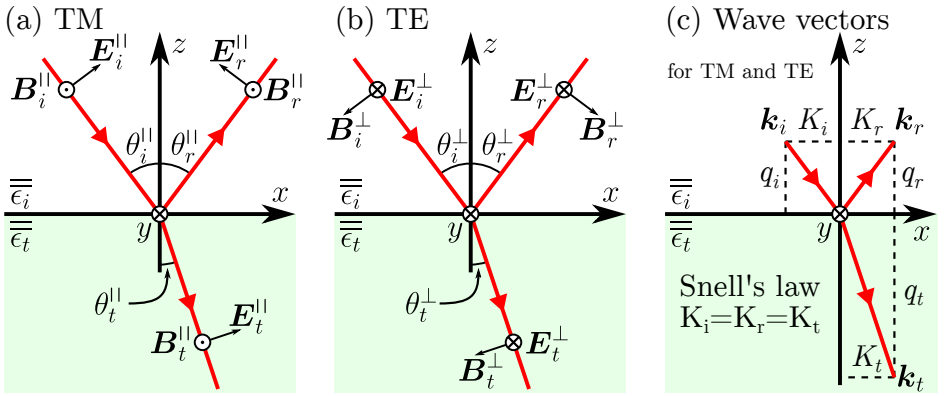


Figure 4.9: Incident ($i$), reflected ($r$) and transmitted ($t$) plane waves at the anisotropic media interface for (a) transverse magnetic ($TM$) and (b) transverse electric ($TE$) polarizations. The wave vectors $\boldsymbol{k}_i$, $\boldsymbol{k}_r$ and $\boldsymbol{k}_t$ for both polarizations are shown in (c), where their x-components are depicted continuous according to the Snell-Descartes law.

coordinate system leads to a translation symmetry in y-direction ($\frac{\partial}{\partial y} \to 0$):

$$-\frac{\partial E_y}{\partial z} = i\omega B_x \qquad -\frac{\partial B_y}{\partial z} = -i\frac{\omega}{c_0^2}\epsilon_o E_x \tag{4.17}$$

$$\frac{\partial E_x}{\partial z} - \frac{\partial E_z}{\partial x} = i\omega B_y \qquad \frac{\partial B_x}{\partial z} - \frac{\partial B_z}{\partial x} = -i\frac{\omega}{c_0^2}\epsilon_o E_y \tag{4.18}$$

$$\frac{\partial E_y}{\partial x} = i\omega B_z \qquad \frac{\partial B_y}{\partial x} = -i\frac{\omega}{c_0^2}\epsilon_e E_z \tag{4.19}$$

The equations on left can be merged with the ones on right by eliminating the vector components of $\boldsymbol{B}$ and substituting $\frac{\omega^2}{c_0^2} = k_0^2$:

$$\frac{\partial^2 E_x}{\partial z^2} - \frac{\partial^2 E_z}{\partial z \partial x} = -k_0^2 \epsilon_o E_x \tag{4.20}$$

$$\frac{\partial^2 E_y}{\partial z^2} + \frac{\partial^2 E_y}{\partial x^2} = -k_0^2 \epsilon_o E_y \tag{4.21}$$

$$\frac{\partial^2 E_z}{\partial x^2} - \frac{\partial^2 E_x}{\partial x \partial z} = -k_0^2 \epsilon_e E_z \tag{4.22}$$

Plane wave approximation decouples Equation 4.21 for y-component from Equations 4.20 and 4.22 for xz-components. Therefore, any field, $\boldsymbol{E}$ can expressed as a sum of its transverse magnetic, $\boldsymbol{E}_{||} = (E_x^{||}, 0, E_z^{||})^T$ and transverse electric $\boldsymbol{E}_{\perp} = (0, E_y^{\perp}, 0)^T$ components.

### Find Ordinary and Extraordinary Propagation Modes

A general plane wave solution for both polarizations is $\boldsymbol{F}(\boldsymbol{r}) = \boldsymbol{F}_0 e^{i\boldsymbol{k}\cdot\boldsymbol{r}} = \boldsymbol{F}_0 e^{iKx+iqz}$. Therefore, all differential operators in Equations 4.20–4.22 can be substituted with $\boldsymbol{\nabla} \to i\boldsymbol{k}$, $\frac{\partial}{\partial x} \to iK$ and $\frac{\partial}{\partial z} \to iq$:

$$-q_{||}^2 E_x^{||} + q_{||} K_{||} E_z^{||} + k_0^2 \epsilon_o E_x^{||} = 0 \tag{4.23}$$

$$-q_{\perp}^2 E_y^{\perp} - K_{\perp}^2 E_y^{\perp} + k_0^2 \epsilon_o E_y^{\perp} = 0 \tag{4.24}$$

$$-K_{||}^2 E_z^{||} + q_{||} K_{||} E_x^{||} + k_0^2 \epsilon_e E_z^{||} = 0 \tag{4.25}$$

This can be elegantly written in a matrix form:

$$\begin{bmatrix} k_0^2\epsilon_o - q_{||}^2 & 0 & q_{||}K_{||} \\ 0 & k_0^2\epsilon_o - q_{\perp}^2 - K_{\perp}^2 & 0 \\ q_{||}K_{||} & 0 & k_0^2\epsilon_e - K_{||}^2 \end{bmatrix} \begin{bmatrix} E_x^{||} \\ E_y^{\perp} \\ E_z^{||} \end{bmatrix} = \overline{\overline{A}}\boldsymbol{x} = 0 \tag{4.26}$$

To permit non-zero $\boldsymbol{x}$ solutions, determinant of matrix $\overline{\overline{A}}$ must be set to zero. In other words, $\det(\overline{\overline{A}}) = (k_0^2\epsilon_o - q_{||}^2)(k_0^2\epsilon_o - q_{\perp}^2 - K_{\perp}^2)(k_0^2\epsilon_e - K_{||}^2) - (q_{||}K_{||})^2(k_0^2\epsilon_o - q_{\perp}^2 - K_{\perp}^2) = k_0^2\epsilon_o(k_0^2\epsilon_o - q_{\perp}^2 - K_{\perp}^2)(k_0^2\epsilon_e - \frac{\epsilon_e}{\epsilon_o}q_{||}^2 - K_{||}^2) = 0$. Ordinary and extraordinary propagation modes, denoted by $\perp$ and $\|$, can be found if the wave vectors for x- and z-components are written as $q = k\cos\theta$ and $K = k\sin\theta$, and substituted back to the equation above: $\det(\overline{\overline{A}}) = k_0^2\epsilon_o(k_0^2\epsilon_o - k_{\perp}^2)(k_0^2\epsilon_e - k_{||}^2[\frac{\epsilon_e}{\epsilon_o}\cos^2\theta_{||} + \sin^2\theta_{||}]) = 0$. Possible propagation modes in azimuthal uniaxial anisotropic medium are:

$$k_{\perp}^2 = k_0^2\epsilon_o \qquad\qquad k_{\perp} = \pm k_0 n_o$$

$$k_{||}^2 = k_0^2 \frac{\epsilon_e\epsilon_o}{\epsilon_e\cos^2\theta_{||} + \epsilon_o\sin^2\theta_{||}} = k_0^2 N(\theta_{||})^2 \qquad k_{||} = \pm k_0 N(\theta_{||})$$

### Determine Incident, Reflected and Trasmitted Wave Fields

Before evaluating the field continuity at interfaces, the field quantities are needed for incident, reflected and transmitted waves. As shown before, the plane wave polarization fields are decoupled and each wave propagates at its own amplitude, $E_{\perp}$ and $E_{||}$, and angle of incidence, $\theta_{\perp}$ and $\theta_{||}$. A required relation between x- and z-components of extraordinary waves is derived using

Equation 4.26 and its determinant solution, $k_0^2\epsilon_e - \frac{\epsilon_e}{\epsilon_o}q_{||}^2 - K_{||}^2 = 0$:

$$E_x^{||} = \frac{k_0^2\epsilon_e - K_{||}^2}{-q_{||}K_{||}}E_z^{||} = \frac{\frac{\epsilon_e}{\epsilon_o}q_{||}^2}{-q_{||}K_{||}}E_z^{||} = -\frac{\epsilon_e q_{||}}{\epsilon_o K_{||}}E_z^{||} = \mp\frac{\epsilon_e\cos\theta_{||}}{\epsilon_o\sin\theta_{||}}E_z^{||}$$

$$E_{||}^2 = {}^{||}E_x^2 + {}^{||}E_z^2 = \left(\mp\frac{\epsilon_e\cos\theta_{||}}{\epsilon_o\sin\theta_{||}}E_z^{||}\right)^2 + {}^{||}E_z^2 = {}^{||}E_z^2\frac{\epsilon_e^2\cos^2\theta_{||} + \epsilon_o^2\sin^2\theta_{||}}{\epsilon_o^2\sin^2\theta_{||}},$$

where $\epsilon_e^2\cos^2\theta_{||} + \epsilon_o^2\sin^2\theta_{||}$

$$= \epsilon_e^2\frac{\epsilon_o}{N(\theta_{||})^2}\frac{N(\theta_{||})^2 - \epsilon_e}{\epsilon_o - \epsilon_e} - \epsilon_o^2\frac{\epsilon_e}{N(\theta_{||})^2}\frac{N(\theta_{||})^2 - \epsilon_o}{\epsilon_o - \epsilon_e}$$

$$= \frac{\epsilon_e\epsilon_o}{N(\theta_{||})^2}(\epsilon_e + \epsilon_o - N(\theta_{||})^2)$$

The sign of the electric field x-component is determined by the sign of the wave vector z-component. Using the field amplitude, the field components can be expressed as:

$$E_z^{||} = \frac{\epsilon_o\sin\theta_{||}}{\sqrt{\epsilon_e^2\cos^2\theta_{||} + \epsilon_o^2\sin^2\theta_{||}}}E_{||} = \frac{\epsilon_o\sin\theta_{||}}{\sqrt{\frac{\epsilon_e\epsilon_o}{N(\theta_{||})^2}(\epsilon_e + \epsilon_o - N(\theta_{||})^2)}}E_{||}$$

$$= \sqrt{\frac{\epsilon_o}{\epsilon_e}}\sin\theta_{||}\frac{N(\theta_{||})}{\sqrt{\epsilon_e + \epsilon_o - N(\theta_{||})^2}}E_{||} = \sqrt{\frac{\epsilon_o}{\epsilon_e}}\sin\theta_{||}A(\theta_{||})E_{||} \tag{4.27}$$

$$E_x^{||} = \mp\frac{\epsilon_e\cos\theta_{||}}{\epsilon_o\sin\theta_{||}}E_z^{||} = \mp\sqrt{\frac{\epsilon_e}{\epsilon_o}}\cos A(\theta_{||})E_{||} \tag{4.28}$$

The signs of each wave vector components are determined by the incident wave vector, $\boldsymbol{k}_i$, and the phase matching condition, also known as the Snell-Descartes law, which states that each wave must have a continuous phase at the media interface, $z = 0$: $\boldsymbol{k_i}\cdot\boldsymbol{r}(z=0) = \boldsymbol{k_r}\cdot\boldsymbol{r}(z=0) = \boldsymbol{k_t}\cdot\boldsymbol{r}(z=0) \Rightarrow K_i = K_r = K_t = K$. The sign convention is shown in Figure 4.9c. In other words, the x-component for each wave vector is equivalent, and hereafter is denoted by $K$. Furthermore, it is found that $k_i\sin\theta_i = k_r\sin\theta_r = k_t\sin\theta_t$, where the wave vectors $k_r$ and $k_i$ are equal. As a consequence, the angle of incidence for both incident and reflected waves is equivalent: $\theta_r = \theta_i$, while the propagation direction is mirrored: $q_r = -q_i$.

After a rigorous and careful derivation, the required electric fields and magnetic flux densities, the former obtained using Equations 4.27–4.28 and the latter derived from the electric fields using Equations 4.17–4.19 and the determinant solution to Equation 4.26, are finally formulated as:

$$\boldsymbol{E}_i = \begin{bmatrix} E_{i,x} \\ E_{i,y} \\ E_{i,z} \end{bmatrix} = \begin{bmatrix} \sqrt{\frac{\epsilon_{i,e}}{\epsilon_{i,o}}} \cos\theta_i^{||} A(\theta_i^{||}) E_i^{||} \exp(iK_{||}x - iq_i^{||}z) \\ E_i^{\perp} \exp(iK_{\perp}x - iq_i^{\perp}z) \\ \sqrt{\frac{\epsilon_{i,o}}{\epsilon_{i,e}}} \sin\theta_i^{||} A(\theta_i^{||}) E_i^{||} \exp(iK_{||}x - iq_i^{||}z) \end{bmatrix}$$

$$\boldsymbol{E}_r = \begin{bmatrix} E_{r,x} \\ E_{r,y} \\ E_{r,z} \end{bmatrix} = \begin{bmatrix} -\sqrt{\frac{\epsilon_{i,e}}{\epsilon_{i,o}}} \cos\theta_i^{||} A(\theta_i^{||}) E_r^{||} \exp(iK_{||}x + iq_i^{||}z) \\ E_r^{\perp} \exp(iK_{\perp}x + iq_i^{\perp}z) \\ \sqrt{\frac{\epsilon_{i,o}}{\epsilon_{i,e}}} \sin\theta_i^{||} A(\theta_i^{||}) E_r^{||} \exp(iK_{||}x + iq_i^{||}z) \end{bmatrix}$$

$$\boldsymbol{E}_t = \begin{bmatrix} E_{t,x} \\ E_{t,y} \\ E_{t,z} \end{bmatrix} = \begin{bmatrix} \sqrt{\frac{\epsilon_{t,e}}{\epsilon_{t,o}}} \cos\theta_t^{||} A(\theta_t^{||}) E_t^{||} \exp(iK_{||}x - iq_t^{||}z) \\ E_t^{\perp} \exp(iK_{\perp}x - iq_t^{\perp}z) \\ \sqrt{\frac{\epsilon_{t,o}}{\epsilon_{t,e}}} \sin\theta_t^{||} A(\theta_t^{||}) E_t^{||} \exp(iK_{||}x - iq_t^{||}z) \end{bmatrix}$$

$$\boldsymbol{B}_i = \begin{bmatrix} B_{i,x} \\ B_{i,y} \\ B_{i,z} \end{bmatrix} = \frac{1}{i\omega} \begin{bmatrix} -\frac{\partial E_{i,y}}{\partial z} \\ \frac{\partial E_{i,x}}{\partial z} - \frac{\partial E_{i,z}}{\partial x} \\ \frac{\partial E_{i,y}}{\partial x} \end{bmatrix} = \frac{1}{i\omega} \begin{bmatrix} iq_i^{\perp} E_{i,y} \\ -iq_i^{||} E_{i,x} - iK_{||} E_{i,z} \\ iK_{\perp} E_{i,y} \end{bmatrix}$$

$$= \frac{1}{\omega} \begin{bmatrix} q_i^{\perp} E_i^{\perp} \exp(\cdots) \\ -[\frac{\epsilon_{i,e}}{\epsilon_{i,o}} q_i^{||} N(\theta_i^{||}) \cos\theta_i^{||} + K_{||} N(\theta_i^{||}) \sin\theta_i^{||}] \sqrt{\frac{\epsilon_{i,o}}{\epsilon_{i,e}}} \frac{A(\theta_i^{||})}{N(\theta_i^{||})} E_i^{||} \exp(\cdots) \\ K_{\perp} E_i^{\perp} \exp(\cdots) \end{bmatrix}$$

$$= \frac{1}{\omega} \begin{bmatrix} q_i^{\perp} E_i^{\perp} \exp(iK_{\perp}x - iq_i^{\perp}z) \\ -k_0 \sqrt{\epsilon_{i,o}\epsilon_{i,e}} \frac{A(\theta_i^{||})}{N(\theta_i^{||})} E_i^{||} \exp(iK_{||}x - iq_i^{||}z) \\ K_{\perp} E_i^{\perp} \exp(iK_{\perp}x - iq_i^{\perp}z) \end{bmatrix}$$

$$\boldsymbol{B}_r = \begin{bmatrix} B_{r,x} \\ B_{r,y} \\ B_{r,z} \end{bmatrix} = \frac{1}{\omega} \begin{bmatrix} -q_i^{\perp} E_r^{\perp} \exp(iK_{\perp}x + iq_i^{\perp}z) \\ -k_0 \sqrt{\epsilon_{i,o}\epsilon_{i,e}} \frac{A(\theta_i^{||})}{N(\theta_i^{||})} E_r^{||} \exp(iK_{||}x + iq_i^{||}z) \\ K_{\perp} E_r^{\perp} \exp(iK_{\perp}x + iq_i^{\perp}z) \end{bmatrix}$$

$$\boldsymbol{B}_t = \begin{bmatrix} B_{t,x} \\ B_{t,y} \\ B_{t,z} \end{bmatrix} = \frac{1}{\omega} \begin{bmatrix} q_t^{\perp} E_t^{\perp} \exp(iK_{\perp}x - iq_t^{\perp}z) \\ -k_0 \sqrt{\epsilon_{t,o}\epsilon_{t,e}} \frac{A(\theta_t^{||})}{N(\theta_t^{||})} E_t^{||} \exp(iK_{||}x - iq_t^{||}z) \\ K_{\perp} E_t^{\perp} \exp(iK_{\perp}x - iq_t^{\perp}z) \end{bmatrix}$$

### Boundary Conditions at Interfaces

The integral form of Maxwell's Equations 4.9–4.12 are valid everywhere, even at the discontinuous interfaces between media, and are useful in obtaining the

continuity relations needed for the anisotropic Fresnel coefficients. However, only the results are shown here because they are equivalent to those described in Chapter 1.5 in *Electromagnetic Waves and Antennas* –book [82].

The Maxwell–Ampère equation together with Gauss' law for magnetism determine the $\boldsymbol{B}$ continuity at interface ($z = 0$): $\boldsymbol{B}_i + \boldsymbol{B}_r = \boldsymbol{B}_t$.

$$q_i^{\perp}(E_i^{\perp} - E_r^{\perp}) = q_t^{\perp} E_t^{\perp} \tag{4.29}$$

$$\sqrt{\epsilon_{i,o}\epsilon_{i,e}}\frac{A(\theta_i^{||})}{N(\theta_i^{||})}(E_i^{||} + E_r^{||}) = \sqrt{\epsilon_{t,o}\epsilon_{t,e}}\frac{A(\theta_t^{||})}{N(\theta_t^{||})}E_t^{||} \tag{4.30}$$

$$E_i^{\perp} + E_r^{\perp} = E_t^{\perp} \tag{4.31}$$

The Maxwell–Faraday equation states the tangential continuity of the electric field $\boldsymbol{E}_T$ at interface ($z = 0$): $\boldsymbol{E}_{T,i} + \boldsymbol{E}_{T,r} = \boldsymbol{E}_{T,t}$

$$\sqrt{\frac{\epsilon_{i,e}}{\epsilon_{i,o}}}\cos\theta_i^{||} A(\theta_i^{||})(E_i^{||} - E_r^{||}) = \sqrt{\frac{\epsilon_{t,e}}{\epsilon_{t,o}}}\cos\theta_t^{||} A(\theta_t^{||})E_t^{||} \tag{4.32}$$

$$E_i^{\perp} + E_r^{\perp} = E_t^{\perp} \tag{4.33}$$

The normal continuity is obtained from Gauss' law, which states that $\epsilon_e \boldsymbol{E}_N$ is continuous at interface ($z = 0$): $\epsilon_{i,e}\boldsymbol{E}_{N,i} + \epsilon_{i,e}\boldsymbol{E}_{N,r} = \epsilon_{t,e}\boldsymbol{E}_{N,t}$

$$\sqrt{\epsilon_{i,o}\epsilon_{i,e}}\frac{A(\theta_i^{||})}{N(\theta_i^{||})}(E_i^{||} + E_r^{||}) = \sqrt{\epsilon_{t,o}\epsilon_{t,e}}\frac{A(\theta_t^{||})}{N(\theta_t^{||})}E_t^{||} \tag{4.34}$$

### Uniaxial Anisotropic Fresnel Coefficients

By defining transmission and reflection coefficients as $t_{\perp} = E_t^{\perp}/E_i^{\perp}$, $t_{||} = E_t^{||}/E_i^{||}$, $r_{\perp} = E_r^{\perp}/E_i^{\perp}$, $r_{||} = E_r^{||}/E_i^{||}$, and substituting dielectric functions with refractive indices, $\epsilon = n^2$ and wavenumbers with $q = k\cos\theta$, Equations 4.29–4.34 can be combined together:

$$n_{i,o}\cos\theta_i^{\perp}(1 - r_{\perp}) = n_{t,o}\cos\theta_t^{\perp} t_{\perp} \tag{4.35}$$

$$1 + r_{\perp} = t_{\perp} \tag{4.36}$$

$$\frac{n_{i,e}}{n_{i,o}}\cos\theta_i^{||} A(\theta_i^{||})(1 - r_{||}) = \frac{n_{t,e}}{n_{t,o}}\cos\theta_t^{||} A(\theta_t^{||})t_{||} \tag{4.37}$$

$$n_{i,o}n_{i,e}\frac{A(\theta_i^{||})}{N(\theta_i^{||})}(1 + r_{||}) = n_{t,o}n_{t,e}\frac{A(\theta_t^{||})}{N(\theta_t^{||})}t_{||} \tag{4.38}$$

Solving the transmission and reflection coefficients result in Fresnel coefficients for uniaxial anisotropic media, where $N$ and $A$ are denoted as $N(\theta_{||}) = n_e n_o / \sqrt{n_e^2 \cos^2\theta_{||} + n_o^2 \sin^2\theta_{||}}$ and $A(\theta_{||}) = N(\theta_{||}) / \sqrt{n_e^2 + n_o^2 - N(\theta_{||})^2}$:

$$r_\perp = \frac{n_{i,o}\cos\theta_i^\perp - n_{t,o}\cos\theta_t^\perp}{n_{i,o}\cos\theta_i^\perp + n_{t,o}\cos\theta_t^\perp} \tag{4.39}$$

$$t_\perp = \frac{2n_{i,o}\cos\theta_i^\perp}{n_{i,o}\cos\theta_i^\perp + n_{t,o}\cos\theta_t^\perp} \tag{4.40}$$

$$r_{||} = \frac{n_{t,o}^2 N(\theta_i^{||})\cos\theta_i^{||} - n_{i,o}^2 N(\theta_t^{||})\cos\theta_t^{||}}{n_{t,o}^2 N(\theta_i^{||})\cos\theta_i^{||} + n_{i,o}^2 N(\theta_t^{||})\cos\theta_t^{||}} \tag{4.41}$$

$$t_{||} = \frac{n_{i,e}A(\theta_i^{||})}{n_{t,e}A(\theta_t^{||})} \frac{2n_{t,o}n_{i,o}N(\theta_t^{||})\cos\theta_i^{||}}{n_{t,o}^2 N(\theta_i^{||})\cos\theta_i^{||} + n_{i,o}^2 N(\theta_t^{||})\cos\theta_t^{||}} \tag{4.42}$$

These reduce to well known Fresnel coefficients for isotropic media in two cases: 1) if $n_e \approx n_o$, then $N$ and $A$ reduce to $n_o$ and 1, or 2) if angle of incidence is near zero, then $N$ reduces to $n_o$ and $A$ to $n_o/n_e$:

$$r_\perp \approx \frac{n_{i,o}\cos\theta_i^\perp - n_{t,o}\cos\theta_t^\perp}{n_{i,o}\cos\theta_i^\perp + n_{t,o}\cos\theta_t^\perp} \qquad t_\perp \approx \frac{2n_{i,o}\cos\theta_i^\perp}{n_{i,o}\cos\theta_i^\perp + n_{t,o}\cos\theta_t^\perp} \tag{4.43}$$

$$r_{||} \approx \frac{n_{t,o}\cos\theta_i^{||} - n_{i,o}\cos\theta_t^{||}}{n_{t,o}\cos\theta_i^{||} + n_{i,o}\cos\theta_t^{||}} \qquad t_{||} \approx \frac{2n_{i,o}\cos\theta_i^{||}}{n_{t,o}\cos\theta_i^{||} + n_{i,o}\cos\theta_t^{||}} \tag{4.44}$$

### Recursion Formulation

Each layer in a multilayer structure exhibits unlimited number of internal reflections, which cause constructive and destructive self-interferences within the structure. A recursive formalism is developed to account for all interference phenomena. Formulation is equivalent for both polarizations and is built on the Fresnel coefficients, $t$ and $r$, and the propagation coefficient, $p = e^{-ikd}$, where $k$ is the propagation mode and $d$ is the distance travelled. Derivation of recursive reflection and transmission coefficients consists of two phases, shown in Figures 4.10a and 4.10b: 1) begin with a simple three layer structure, where a finite layer is sandwiched between two semi-infinite layers, and 2) generalize recursively to a multilayer structure.

As can be deduced from Figure 4.10a, the reflected and transmitted electric fields, $E_r$ and $E_t$, can be expressed as a sum of their internal reflection

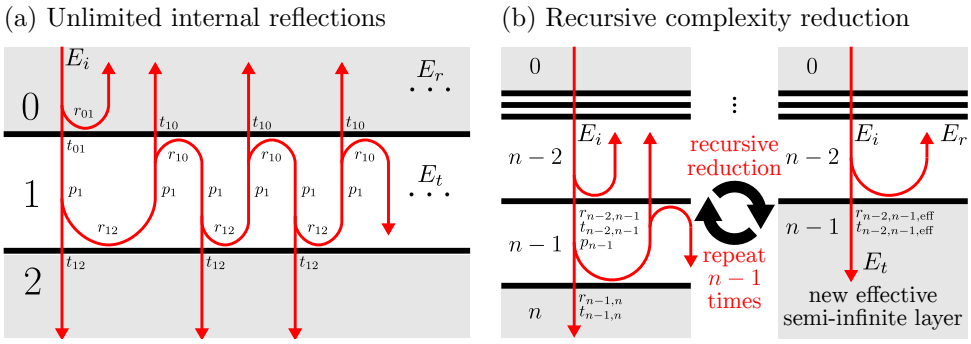


Figure 4.10: Plane wave self-interferences in multilayer structure. Semi-infinite layers are marked with gray. (a) Unlimited number of internal reflections in a simple structure. (b) A general case, where the layer number is recursively reduced by using effective coefficients.

contributions with respect to the incident electric field amplitude, $E_i$:

$$\begin{aligned} E_r &= E_i r_{01} + E_i t_{01} p_1 r_{12} p_1 \cdot t_{10} + E_i t_{01} p_1 r_{12} p_1 \cdot r_{10} p_1 r_{12} p_1 \cdot t_{10} + \dots \\ &= E_i r_{01} + E_i t_{01} p_1 r_{12} p_1 \underbrace{(1 + r_{10} p_1 r_{12} p_1 + \dots)}_{\sum_{k=0}^{\infty} (r_{10} p_1 r_{12} p_1)^k} t_{10} \end{aligned} \tag{4.45}$$

$$\begin{aligned} E_t &= E_i t_{01} + E_i t_{01} \cdot p_1 r_{12} p_1 r_{10} + E_i t_{01} \cdot p_1 r_{12} p_1 r_{10} \cdot p_1 r_{12} p_1 r_{10} + \dots \\ &= E_i t_{01} \underbrace{(1 + p_1 r_{12} p_1 r_{10} + \dots)}_{\sum_{k=0}^{\infty} (p_1 r_{12} p_1 r_{10})^k} \end{aligned} \tag{4.46}$$

Infinite sums in Equations 4.45 and 4.46 are recognized as converging geometric series, which can be replaced with $\sum_{k=0}^{\infty} ar^k = \frac{a}{1-r}$, for $|r| < 1$:

$$E_r = E_i \left( r_{01} + \frac{t_{01} p_1 r_{12} p_1}{1 - r_{10} p_1 r_{12} p_1} t_{10} \right) = E_i r_{01,\text{eff}} \tag{4.47}$$

$$E_t = E_i \left( \frac{t_{01}}{1 - p_1 r_{12} p_1 r_{10}} \right) = E_i t_{01,\text{eff}} \tag{4.48}$$

As a consequence, the effective reflection and transmission coefficients, $r_{01,\text{eff}}$ and $t_{01,\text{eff}}$, introduced in Equations 4.47 and 4.48, merge the two bottom layers into a new effective semi-infinite layer. In other words, any multilayer structure can be recursively reduced to a two layer structure, as can be concluded from Figure 4.10b. This is accomplished by recursively replacing the two current bottom layers with a new semi-infinite layer, which has the Fresnel coefficients replaced with the effective coefficients and includes all contributions to interference that occur below this layer. Therefore, the

general effective reflection and transmission coefficients for arbitrary layer-indices, $i, j = i + 1, k = i + 2 \in \aleph$, are written as:

$$r_{ij,\text{eff}} = r_{ij} + \frac{t_{ij} p_j r_{jk,\text{eff}} p_j}{1 - r_{ji} p_j r_{jk,\text{eff}} p_j} t_{ji} \qquad t_{ij,\text{eff}} = \frac{t_{ij}}{1 - p_j r_{jk,\text{eff}} p_j r_{ji}} \tag{4.49}$$

### Numerical Model

The derived coefficients in Equation 4.49 are then used to calculate enhancement factors, hereafter denoted as $F$, which determine how the incident electric field changes by passing through the finite part of the multilayer structure. For this work, graphene and silicon oxide were considered finite, while air and silicon were semi-infinite. In the Si-peak model, the enhancement factors $F_{\text{ab}}(\theta, z) = t_{23,\text{eff}} \cdot p_2 \cdot t_{12,\text{eff}} \cdot p_1 \cdot t_{01,\text{eff}}$ and $F_{\text{sc}}(\theta, z) = t_{10,\text{eff}} \cdot p_1 \cdot t_{21,\text{eff}} \cdot p_2 \cdot t_{32,\text{eff}}$ for absorbing and scattering wavelengths, respectively, are were calculated for both polarizations by permuting the angle of incidence, $\theta$ and the number of graphene layers, $z$. As the scattered light propagates backwards, it sees the multilayer structure inverted.

In spectroscopy, the electric field amplitude of the scattered light is indirectly obtained via the measured light irradiance. In this work it is denoted as intensity, $I = \langle |\boldsymbol{S}| \rangle$, and is time-averaged magnitude of the Poynting vector, $\boldsymbol{S} = (2\mu_0)^{-1} \operatorname{Re}\{\boldsymbol{E} \times \boldsymbol{B}^*\}$. A solution for plane waves propagating in isotropic lossy medium is expressed as $I = \frac{\operatorname{Re}\{n\}}{2\mu_0 c_0} |E|^2 e^{-2 \operatorname{Im}\{n\} k_0 \hat{\boldsymbol{k}} \cdot \boldsymbol{r}}$. The relation for anisotropic medium is even more complicated as has been shown by S. J. Orfanidis in his book, chapter 4.6 and equation 4.6.29 [82]. This, along with the angle dependent lossy term, are avoided in the Si-peak model by evaluating the intensity only in air, which is isotropic low-loss medium.

By taking the approximations described in Section 4.5.1 into consideration, the Si-peak intensity can then be expressed in integral form: $I(z) = \frac{1}{2I_0} \int_0^{\theta_{max}} |E_i^{||}(\theta) F_{\text{ab}}^{||}(\theta, z) F_{\text{sc}}^{||}(\theta, z)|^2 + |E_i^{\perp}(\theta) F_{\text{ab}}^{\perp}(\theta, z) F_{\text{sc}}^{\perp}(\theta, z)|^2 d\theta$, where $z$ is the number of graphene layers, $I_0$ is the normalizing term so that $I(0) = 1$, $\theta_{max}$ is the maximum angle of incidence, $E_i$ is the incident light electric field, and $F_{\text{ab}}$ and $F_{\text{sc}}$ are the previously defined enhancement factors. The Si-peak analysis is then carried out by evaluating this integral with sub-layer resolution for known laser wavelength, lens numerical aperture and the Si-peak Raman shift, and determining the number of graphene layers via interpolation as explained in Section 4.3.2.

## 4.6 Reliability Verified via Cross-Correlation

To demonstrate the model reliability, the model output was cross-correlated with a FLG thickness reference, constructed using the combined information from other sources, and an AFM scan data. A cross-correlation between two maps creates a scatter plot, where each axis represents the corresponding map value range. Cross-correlation between $N$ maps generates $N(N-1)/2$ unique scatter plots. The cross-correlation between model output and other Raman spectral features was also studied to strengthen the reliability by reproducing the previous research observations.

### 4.6.1 FLG Thickness Reference

A number-of-layers reference for FLG was manually constructed by performing a careful analysis on each few-layer area on every sample. Following Raman-based layer-number fingerprints, shown in Table 2.2, were analysed: FWHM(2D), Pos(2D), Shape(2D), Ratio–I(2D, G) and I(G). While SLG, BLG and 3-LG are generally easily distinguished by the Shape(2D) analysis alone, other fingerprints provide important clues in making the decision on 4-LG and 5-LG with considerable noise. For even thicker areas, the number of layers may be deduced from a possible graphene folding.

To aid the more complex spectral shape analysis of the 2D-peak, a computer assisted data-to-data fitting was performed. The Shape(2D) data for 532 nm excitation on the ABA- and ABC-stacked FLG, collected by Nguyen et al. [78], was obtained by a careful digitization. Before the fitting, the Rayleigh-peak was recalibrated in order to ensure accurate spectral positions. This permits the data-to-data fitting to fix the Raman shift axis. The intensity axis offset and scaling was kept floating because Nguyen et al. had 100 nm $SiO_2$ and, hence, operated in different interference regime [101]. Once each FLG area was spectral averaged, recalibrated and fitted, the number of layers and the stacking order were determined via visual comparison of the fitting results, which also displayed the coefficient of determination ($R^2$) and the sum of squared errors ($SSE$) goodness-of-fit parameters.

### 4.6.2 AFM Scan Data

Several samples were AFM-scanned to evaluate the model capabilities beyond FLG. It was found that the graphene thickness values for FLG obtained from a carefully levelled AFM data, deviated from the expected, demanding an explanation to the anomaly. Moreover, the AFM scan data was pre-processed

to permit a direct correlation study with Raman measurements. The data processing and the major error sources are discussed in this subsection.

First, the AFM scan data is levelled and substrate level set to 0 nm. Second, the data is carefully overlaid with the corresponding Si-peak intensity scan data by visually inserting three control points to each map. Finally, the AFM data is affine transformed to Raman coordinate system, usually downscaling in the process.

There are four major error sources for AFM to be taken into consideration: 1) Imperfect levelling of the scan data distortions leads to considerable deviation when determining the number of graphene layers. 2) Tapping-mode AFM produces a visible anomalous offset with FLG [36, 61, 77]. 3) Misalignment in the map-to-map overlay, caused by human error, generates a feature mismatch. 4) Error near the graphene edges, occurring even in perfect alignment, due to naturally emerging spatially wider gradient at the edge in Raman compared to that of AFM.

# Chapter 5

# Results & Discussion

## 5.1 Si-Peak Analysis for Pristine Graphene

### 5.1.1 285 nm Oxide Thickness

The objective in this work was to determine the number of graphene layers using the Si-peak analysis of mechanically exfoliated graphene transferred on 285 nm $SiO_2$/Si–substrates, which were cut from the wafer obtained as-fabricated. First, the calculated number of graphene layers was compared to the FLG thickness reference, described in Section 4.6.1, up to 10 layers. Second, the model output was cross-correlated with other well known Raman-based layer-number fingerprints, introduced in Table 2.2, such as FWHM(2D), Pos(2D), Ratio–I(2D, G) and Ratio–I(G, $Si_G$).

In Figure 5.1a, the estimated number of graphene layers is cross-correlated with the FLG thickness reference. The Si-peak model parameters were as follows: 532.1 nm excitation wavelength, 285 nm oxide thickness and 0.95 NA. Before the analysis the Si-peak intensities were area-averaged. It is found that the model shows an excellent agreement with the reference up to 10 layers and follows the eye guiding 1:1–line. Some variance is evident in the plot, especially at 3 layers, what is attributed to the original $SiO_2$/Si–wafer non-uniformity. The visible gap between 5 and 10 layers is due to the absence of the folded graphene in the FLG thickness reference. The only 10-LG area was determined via a careful analysis of the folding geometry.

The Si-peak intensity was modelled as a function of the number of layers in Figure 5.1b. The log-linear plot up to 300 layers clearly depicts the non-linear behaviour of the three Si-models with 275 nm, 285 nm and 295 nm oxide. These models were plotted to explain the variance due to the oxide non-uniformity, as discussed in the previous paragraph. However, this graph is partially incomplete as it lacks the Si-peak intensity information beyond

(a) Model vs. the FLG thickness reference (b) Si-peak intensities modelled

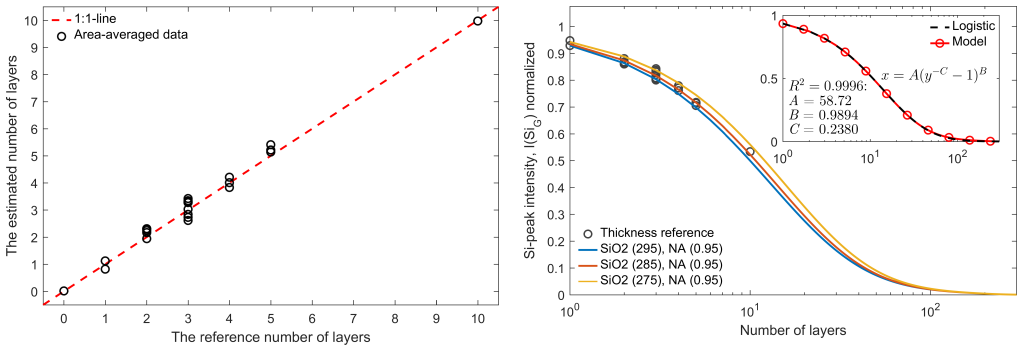


Figure 5.1: Analysis of area-averaged Si-peak intensities, I($Si_G$), each point representing a N-LG area on 285 nm $SiO_2$/Si–substrate. (a) Comparison between the reference number of layers and that of the model. Dashed line is the eye guiding 1:1–line and represents a perfect cross-correlation. (b) Si-peak intensities modelled using three different oxide thicknesses: 295 nm (blue), 285 nm (red) and 275 nm (yellow). Inset compares the model to a fitted inverse of log-transformed asymmetric logistic function, $x = A(y^{-C} - 1)^B$.

10 layers. This shortcoming is complemented later in Section 5.1.2 with the AFM scan data obtained for a stairway-like graphene flake on 365 nm oxide.

Inset in Figure 5.1b demonstrates that the correlation between the Si-peak model and the observations can be semi-empirically approximated with a simple three-parameter inverse of log-transformed asymmetric logistic function, $x = A(y^{-C} - 1)^B$, where $x$ and $y$ denote the number of layers and the normalized Si-peak intensity, respectively. The best fit ($R^2 = 0.9996$) was found using parameter values: $A = 58.72$, $B = 0.9894$ and $C = 0.2380$. This semi-empirical model can then be used to obtain a quick on-site estimate of the number of graphene layers on 285 nm $SiO_2$/Si–substrate.

### Comparison to Other Raman Methods

The Si-peak analysis of the same samples was also compared to four well known Raman methods to determine the number of layers in Figure 5.2a–d: a) FWHM(2D), b) Pos(2D), c) Ratio–I(2D, G) and d) Ratio–I(G, $Si_G$). For clarity, each method was separated into two plots: the one on top displays the area-averaged values and the one of bottom the Raman map pixel values. These results are discussed in the subsequent paragraphs. Although not discussed in this work, the comparison was also done for 365 nm in Figure A.3.

In Figure 5.2a, the FWHM(2D) shows a weak dependence on the number

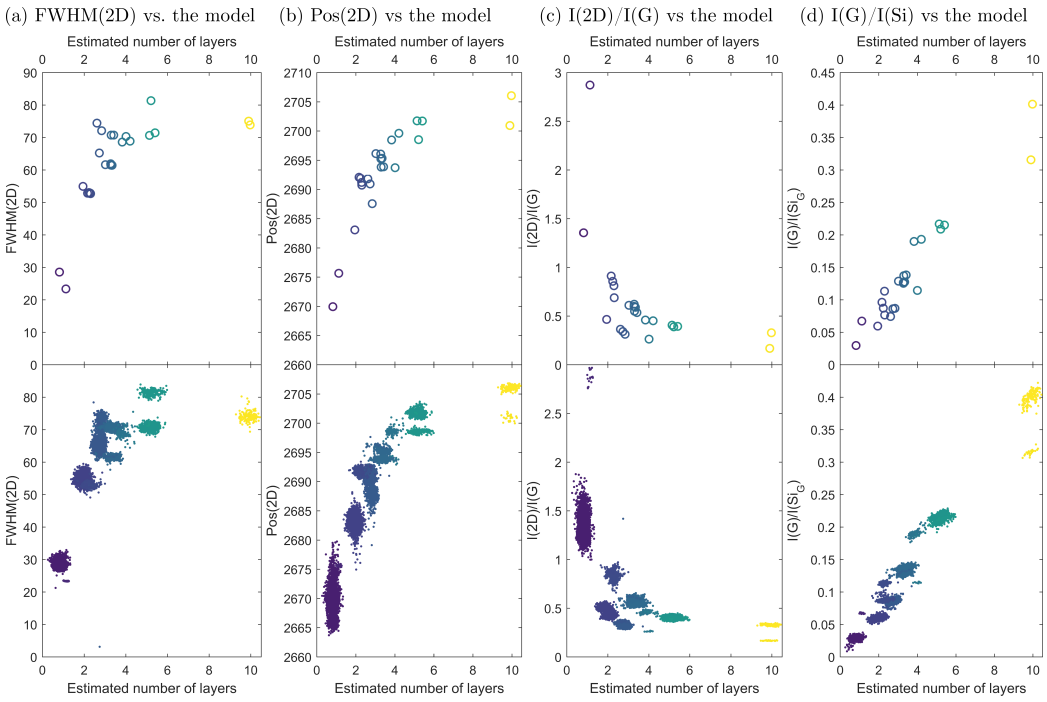


Figure 5.2: Number of graphene layers obtained via the Si-peak analysis for pristine graphene on 285 nm $SiO_2$/Si–substrate correlated with four well known Raman layer-number fingerprints in determining the number of layers: a) FWHM(2D), b) Pos(2D), c) Ratio–I(2D, G) and d) Ratio–I(G, $Si_G$). The plots on top depict the area-averaged values in samples. The plots on bottom represent the raw pixel-to-pixel correlation. The data colouring corresponds to the number of layers: the lighter the shade, the thicker the graphene.

of layers and is not useful after 5 layers as it is saturated to ∼75 $cm^{-1}$. Most of the observed values are similar to the previously reported data [38]. However, few anomalous higher values were found at 3 and 5 layers, ∼70 $cm^{-1}$ and ∼80 $cm^{-1}$, respectively. They arise at the ABC-stacked areas found in the two flakes depicted later in Figure 5.3. This demonstrates that FWHM(2D) can only be used determine the number of ABA-stacked layers, while the Si-peak analysis remains immune to these deviations, as shown in Figure 5.1a.

The spectral position of the 2D-peak in (b) behaves like the FWHM(2D), saturating already at 4 layers to ∼2706 $cm^{-1}$. Most of the observations agree with previously reported values [46]. However, some anomalously low values for 3, 4 and 5 layers are ∼2688 $cm^{-1}$, ∼2694 $cm^{-1}$ and ∼2699 $cm^{-1}$, respectively. The ABC-stacking is known to result in 1–3 $cm^{-1}$ decrease in the Pos(2D) compared to that of the ABA-stacking with same number of layers. A closer examination of the data reveals that one of the samples with

1–3 layers show overall decrease of ∼5 $cm^{-1}$, which cannot be attributed to the stacking order only. This anomalous sample is further discussed in the following paragraphs. Moreover, the low value for 10 layers, ∼2701 $cm^{-1}$ originates from the folded graphene, which has random stacking. As the Pos(2D) is known to be stacking order sensitive [46], the Pos(2D) values were expected to be cluttered by the non-ABA-stacked areas. However, as shown in Figure 5.1a, the Si-peak analysis remains insensitive because the Si-peak signal originates from below the graphene.

Figure 5.2c shows the relationship between the Ratio–I(2D, G) and the number of layers. This ratio has a prompt saturation after 3 layers, which severely limits its usage in determining the number of layers. There seems to be two distinguishable curves within the data in (c). After a closer examination of the data, the curves cannot be explained by the ABC-stacked areas, because they seem to be produce similar ratios to that of the ABA-stacked areas. It has been previously reported that the 2D/G intensity ratio is sensitive to the oxide thickness [101]. The sensitivity of the Si-peak analysis to the oxide thickness is also considered in this work in Section 4.3.4 and is depicted in Figure 4.6. It was found that one FLG sample, later presented in Figure 5.3, has lower overall Ratio–I(2D, G) than others, indicating a reduced oxide thickness. This conclusion is supported by a subtle overall decrease in the calculated number of layers for the bottom curve compared to that of the top curve in the plot on top. Therefore, the bottom curve, originating fully from a single anomalous sample, is due to the reduced oxide thickness compared that of others. Interestingly, it is the same anomalous sample as in the Pos(2D) case. While the Ratio–I(2D, G) is fairly sensitive to the variation in the oxide thickness, the Si-peak analysis remains robust against it, as was also calculated previously in Section 4.3.4.

The linearity of the Ratio–I(G, $Si_G$) is depicted in Figure 5.2d, what is very useful in determining the number of layers. A closer examination reveals that the data shows two linear lines. The deviation is attributed to the oxide thickness difference, as previously discussed for the Ratio–I(2D, G). The overall G-peak intensity for one of the samples, same as in two previous cases, is found to be ∼30 % higher than that of others. In other words, if the other samples had ∼300 nm oxide, then this sample would have ∼285 nm according to previous work [101]. It is plausible since the other samples are older and have, however uncertain, either 285 nm or 300 nm oxide. Nevertheless, it is demonstrated here that despite its linearity the Ratio–I(G, $Si_G$) limited by its sensitivity to the oxide thickness variation near 285 nm thickness, while the Si-peak analysis remains stable. Moreover, the I(G)/I($Si_G$) will fail for the random-stacked graphene as it relies on the G-peak intensity, which is altered by the rotational-angle dependent Van Hove singularities [39, 52, 71].

### Bernal and Rhombohedral Stacking Orders

The preceding results show that the Si-peak analysis is insensitive to the stacking order. This is examined here in detail using two FLG flakes on 285 nm oxide, which are depicted in Figure 5.3 using (a) optical micrograph, (b) the Si-peak modelled number of layers and (c) the FWHM(2D) map. The area-averaged Raman spectra in (d) show the G- and 2D-bands for 10 different areas, (1)–(10). The flake on top has the folded 10-LG area at (10) and the flake on bottom has the previously discussed anomalous oxide thickness. Both flakes have ABA- and ABC-stacked areas, which were determined using previously reported analysis [18, 78]. The ABC-stacked areas, for example (4), (7) and (9) labelled with black, have increased FWHM(2D) and are easily distinguishable from the FWHM(2D) maps in (c). However, they nor the folded 10-LG area at (10) are not seen in the calculated number of layers in (b). The given examples provide further evidence that the Si-peak model calculated number of layers remain unaffected by the ABC-stacking.

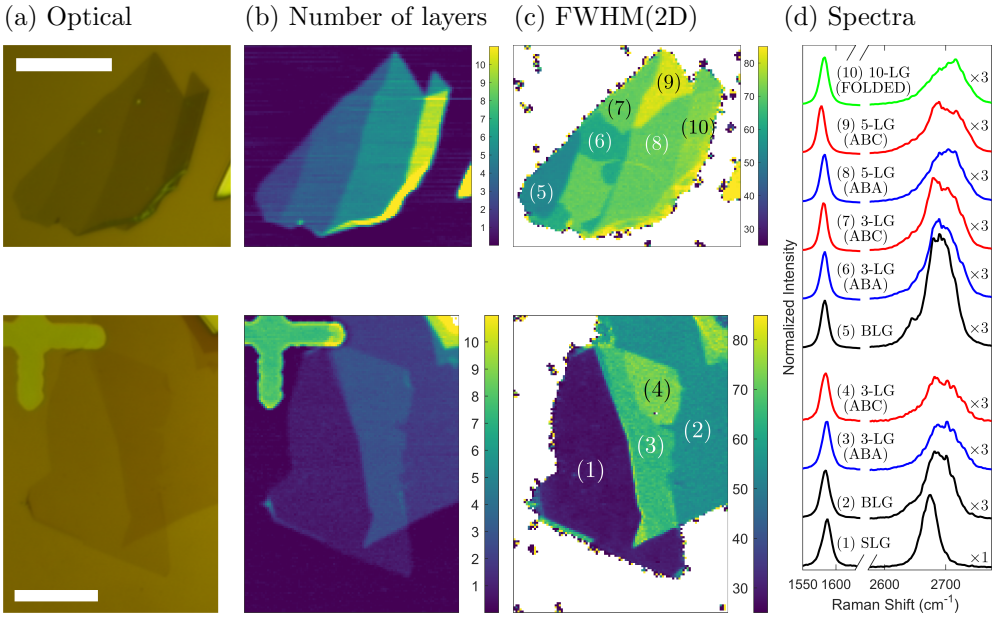


Figure 5.3: Insensitivity of the Si-peak analysis to the stacking order shown using two FLG flakes. (a) Optical images of the FLG flakes with green light filtering. (b) Calculated number of graphene layers using 285 nm $SiO_2$/Si–substrate. (c) ABA- and ABC-stacked areas made visible using FWHM(2D). The folded and ABC-stacked areas are labelled with black. (d) Area-averaged spectra of the labelled areas, (1)–(10). All the 2D-bands were multiplied by 3 excluding the SLG. White scale bars in (a) are 10 $\mu$m long.

### 5.1.2 Effect of Oxide Thickness

The Si-peak analysis was tested beyond 285 nm oxide thickness, discussed in Section 5.1.1, by investigating how well the model covers the Si-peak intensity behaviour as a function of the oxide thickness. Two straightforward tasks were carried out: 1) An oxide etch test, where $I(Si_0)$ was directly Raman measured for various oxide thicknesses, 0–400 nm. 2) The Si-peak analysis for pristine graphene on 365 nm $SiO_2$/Si–substrate, where the Ratio–$I(Si_G, Si_0)$ was measured. Both experimental results were then compared with the Si-peak model.

The oxide etch test results are shown in Figure 5.4a. The Si-peak models with various NA were fit to the observations by varying only the scale of their $I(Si_0)$-axes. The NA values 0.40, 0.75 and 0.95 approximately correspond to 20×, 50× and 100× lenses, respectively. It is interesting that the model with correct NA = 0.95 parameter shows an excellent agreement with the data. This implies that the underlying theory behind the Si-peak analysis is sufficient to explain the oxide thickness dependent features in the Si-peak intensity at the substrate. Moreover, the models show a slight systematic horizontal offset compared to the observed data, which may arise for example from a 2–3 % systematic relative error in the film thickness ellipsometry. Another finding is that the Si-peak intensity for 100 nm would be ∼5 % higher than that of 285 nm, what gives a minor improvement in the image scans using low integration time.

Figure 5.4b displays the Ratio–$I(Si_G, Si_0)$ obtained for pristine graphene on 365 nm oxide. The number of layers are determined using the FLG thickness reference up to 4 layers and using the AFM scan data beyond. The FLG portion of the AFM scan data is cut-off for clarity because AFM has an anomalous offset on graphene as discussed in Section 4.6.2. Same subsection explains the cause to the visible horizontal and vertical anomalies in the scatter plot. The intensity variance for the FLG thickness reference is attributed to the spatial thickness non-uniformity of the original 365 nm $SiO_2$/Si–wafer, from which the substrates were cut from. The Si-peak intensity noise can be reduced by area averaging when evaluating large flat areas. For this work, the noise was only reduced for FLG because most of the Si-peak data for thicker were obtained for a single stairway-like graphene flake.

Three Si-peak models were plotted with the observations in Figure 5.4b using 355, 365 and 375 nm oxide thicknesses. The dark shaded AFM data has accounted for a 10-layer anomalous offset, while the light shaded AFM data in the background shows such an anomaly. It is shown that the model with 355 nm oxide fits best, which is in an apparent contradiction with the measured film thickness, 365 nm. If the ellipsometer, used for thickness

(a) I($Si_0$) versus the $SiO_2$ etch test

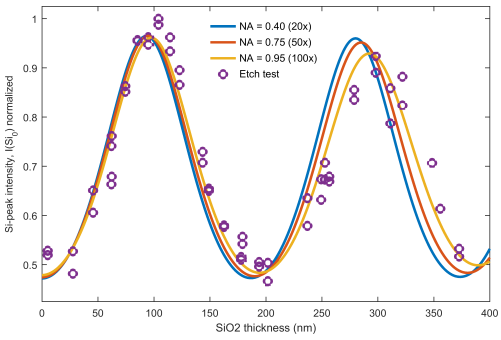


(b) I($Si_G$)/I($Si_0$) for 365 nm $SiO_2$/Si

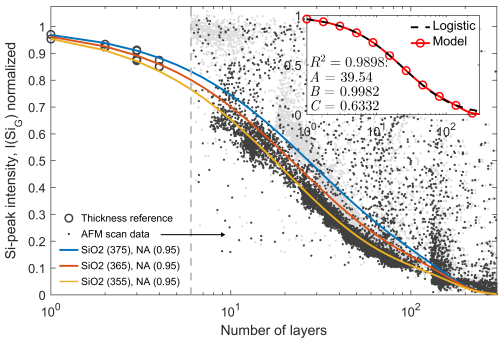


Figure 5.4: Oxide thickness effect on the Si-peak intensities. (a) compares the Si-peak model with observations obtained for a $SiO_2$ etch test. Bare oxide was gradually etched with buffered hydrofluoric acid and thickness measured with an ellipsometer. Two point scans of Si-peak intensity, I($Si_0$) per sample were taken through a 100× objective lens with NA 0.95. (b) shows a log-linear comparison between the model and the combined observations for graphene on 365 nm $SiO_2$/Si–substrate. The thickness data consists of the reference number of layers for FLG and the AFM scan data for $N > 5$. The intensity data is area-averaged before the vertical dashed separator line. Dark shaded AFM scan data is shifted by an anomalous offset of 10 layers from the light shaded raw data in the background. Inset compares the model to the logistic.

estimation, was systematically overestimating the thickness by ∼2.5 %, it would account for the 10 nm thickness mismatch. Interestingly, according to the oxide etch test, the relative error is likely to be within 2–3 %. However, as evident in Figure 5.4b, the anomalous AFM offset of ∼10 layers must be accounted for to obtain an excellent fit. Offset of 10 layers is approximately ∼3.5 nm, of which ∼1.5 nm is the measured anomalous offset for SLG, similar to the previously reported offsets [36, 61, 77], and the rest can originate for example from the user error in manual leveling. In other words, the true oxide thickness of the stairway-like flake is likely to be ∼355 nm. The Si-peak analysis withstands a direct comparison with the AFM scan data, performing better for FLG, due to lack of an offset, and has a good overlap, despite the noise, for thicker.

Inset in Figure 5.4b compares a fitted semi-empirical logistic model, introduced in Section 5.1.1, to the Si-peak model for 365 nm oxide thickness. It is found to be in an excellent agreement ($R^2 = 0.9898$) up to 100 layers using parameter values: $A = 39.54$, $B = 0.9982$ and $C = 0.6332$. However, unlike 285 nm oxide thickness, the Si-peak intensity for 365 nm has addi-

tional non-linear behaviour beyond 100 layers, which the logistic function is unable to account for.

## 5.2 Turbostratic CVD Graphene

The Si-peak analysis was performed for CVD graphene with turbostratic BLG islands transferred on 365 nm $SiO_2$/Si–substrate. Turbostratic, hereafter denoted as random stacking, means any stacking order, where the graphene layers are out of alignment and are randomly orientated relative to each other. Random stacking is of particular interest because in that case most other Raman-based methods to determine the number of graphene layers fail, while the Si-peak analysis should, in theory, be applicable. In addition, although ABA-stacking is sought after in multilayer CVD graphene, the multilayer samples often contain randomly stacked layers.

Figure 5.5 depicts the Si-peak analysis on two random-stacked BLG islands. This is a simple demonstration that any Raman-based method relying on either G- or 2D-peak to determine the number of layers will fail for the random-stacked graphene. Moreover, it is shown in (c) and (g) that the Si-peak analysis is not sensitive to the stacking order and performs well even for tiny random-stacked islands of CVD graphene under extremely noisy conditions. For clarity, the SEM images, the Ratio–I(2D, G) and spectra at three points per sample are given along with the estimated number of layers. The data was received as-measured from other study, where the G-peak intensity was initially maximized, although at the expense of the Si-peak intensity optimality according to Figure A.1. This explains the high noise in the Si-peak intensity and the estimated number of layers. Overall noise is attributed to the short integration time. The blurriness of Raman maps emerge from the fact that the pixel diameters are much smaller than the diffraction limit, as the islands are only $\sim$2 $\mu$m in diameter, and the original signal is convolved with the laser beam point spread function. Furthermore, as is seen from the SEM image (e), the island on bottom has a tiny 3-LG in its centre, what explains the bright spot in (g).

The random-stacked area at (3) of the island on top in Figure 5.5 shows a 20-fold amplification of the G-peak intensity and a doubled 2D-peak with respect to those of at (2), what leads to an unusual one order of magnitude smaller Ratio–I(2D, G). According to the amplified I(G), the rotational angle at (3) is around 10–15°, where 10–30$\times$ amplifications has previously been reported [39, 52]. The island on bottom at (6) shows a slight increase in the G-peak and a 3-fold amplification of the 2D-peak intensity with respect to those of at (5), leading to an abnormally high Ratio–I(2D, G). Previous

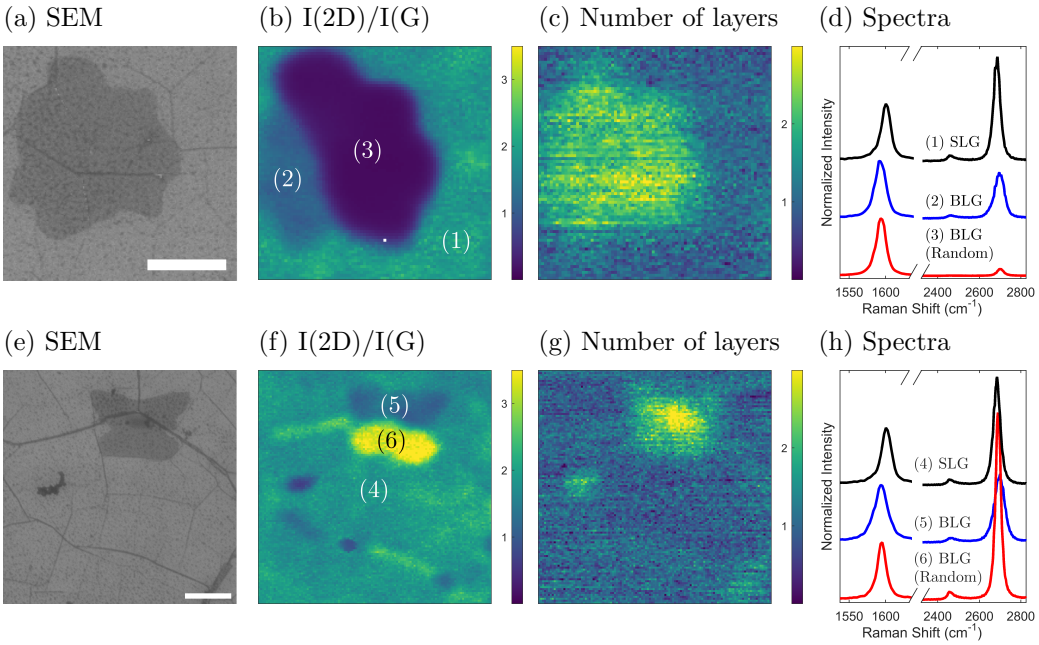


Figure 5.5: Random-stacked CVD graphene islands on 365 nm $SiO_2$/Si–substrate. Images in four columns, (a) and (e), (b) and (f), (c) and (g), and (d) and (h), are as follows: i) SEM images of BLG islands, ii) well known 2D/G intensity ratios, iii) the model calculated number of layers, and iv) the area-averaged spectra of random-stacked BLG offset with regular BLG and SLG. White scale bars in (a) and (e) are 1 $\mu$m long. The Ratio–I(2D, G) for random stacking in (b) is an order of magnitude smaller than that of normal BLG, and, in (f), half decade higher. The calculated average number of layers were 1.0055 and 2.0697 for SLG and BLG areas in (c), and 1.9493 and 1.0100 for SLG and BLG areas in (g). Panels (d) and (h) show the effect of random stacking on the 2D- and G-bands normalized with respect to the G-peak.

work implies that the rotational angle at (6) is 20° or higher [52]. Moreover, the rotational angles around 10–15° show an additional angle-dependent optical absorption peak within the visible spectrum [71, 87]. It might pose a problem to the Si-peak analysis if the absorption is enhanced at the Si-peak wavelength. This narrow range of rotational angles is the only known case where the Si-peak analysis might fail. However, the result in (c) indicates no effect on the Si-peak analysis at (3). Therefore, it is worthwhile to study the matter further in order to determine if the critical rotational angle can restrict the use of the Si-peak analysis.

# Chapter 6

# Summary

Graphene is one-atom thick two-dimensional allotrope of carbon with many unique properties. Pristine monolayer graphene can be obtained from graphite using mechanical exfoliation, which is used in the experimental research. CVD synthesized is more suitable for industrial purposes as it enables fabrication of large-area monolayer graphene. Raman spectroscopy is the most versatile method in the material characterization of graphene. Many properties of graphene, including defects, doping, stacking order and strain, can be analysed from the Raman spectrum of graphene based on well-defined fingerprints of for example the G-, 2D- and D-peak. As vast amount of structural information is packed within the graphene spectrum, it can even be used to determine the number of layers, which was the main objective of this work. However, the main problem in using the Raman methods based on the graphene spectrum to determine the number of layers is that their use is limited by several factors such as the saturation, the stacking order and the substrate. The Si-peak analysis presented in this work was developed to address many of these fundamental limitations.

The Si-peak analysis is a non-destructive Raman-based method to determine the number of graphene layers via the normalized main Si-peak intensity, also denoted Ratio–I($Si_G$, $Si_0$). It was normalized with respect to the Si-peak intensity at the bare substrate, I($Si_0$). As graphene is often transferred on $SiO_2$/Si–substrate, the Si-peak intensity data is also collected during the Raman measurement. The model was carefully described and rigorously derived for graphene on $SiO_2$/Si–substrate in Chapter 4, and was tested using pristine and CVD graphene in Chapter 5. To build upon the already reported information [61], this work was set to assess the model sensitivity to the oxide thickness and the stacking order.

The evaluation was conducted mainly for graphene on 285 nm oxide, where the model output was compared first to the FLG thickness reference

and then to four other Raman methods in Table 2.2 based on evaluation of graphene Raman bands: FWHM(2D), Pos(2D), Ratio–I(2D, G) and Ratio–I(G, $Si_G$). It was found that each of the four methods were either sensitive to the stacking order or the variation in the oxide thickness, while the Si-peak analysis remained insensitive and extracted the correct number of layers in each case. The closer examination of the model performance using the two FLG flakes with varying stacking orders further reinforced that the calculated number of layers are correct. A simple but precise semi-empirical logistic model, $x = A(y^{-C} - 1)^B$ was fit to the Si-peak model to permit a quick on-site estimation of the number of layers up to 100 layers. Here $x$ and $y$ denote the number of graphene layers and the Ratio–I($Si_G$, $Si_0$), respectively.

Moreover, the theoretical grounds of the Si-peak intensity model were analysed further in Section 5.1.2 by comparing the calculated intensity to 1) the observed I($Si_0$) for various oxide thicknesses, 0–400 nm, and 2) the observed Ratio–I($Si_G$, $Si_0$) for graphene on 365 nm oxide, in addition to the results for 285 nm oxide. The model displays an exceptional agreement with the observations in both cases after accounting for the systematic error in ellipsometry and the anomalous AFM offset.

The model sensitivity to the random stacking order in multilayer CVD graphene was examined in Section 5.2 using two CVD graphene islands on 365 nm $SiO_2$/Si–substrate. The results indicated that the Si-peak analysis is unaffected even near the critical rotational angle around 10–15°, where the Raman band relationships of graphene break down due to the resonance [39, 52]. However, a more thorough examination would be interesting in order to verify if the Si-peak analysis applies exactly at the critical rotational angle.

The results in this work indicate that the Si-peak analysis can be used to determine the number of graphene layers on various oxide thicknesses up to 100 layers and is applicable to the ABA-, ABC- and random-stacked graphene. As the Si-peak intensity originates from below, it remains almost entirely insensitive to the varying graphene properties it passes through. This is unlike most other Raman-based methods, which are limited to FLG or the ABA-stacking [52, 87], and are easily distorted by the variation in the oxide thickness [101] or the laser beam focus depth as reported in Figure A.1. In addition, the Si-peak analysis is a promising alternative to AFM as it is completely void of any artefacts and offsets like in AFM [36, 61, 77], and the Si-peak data is usually already included with the other Raman information.

Due to its wide applicability and excellent robustness for graphene, the Ratio–I($Si_G$, $Si_0$) expandability to cover other 2-D crystals transferred on $SiO_2$/Si–substrate, such as hexagonal boron nitride, phosphorene and silicene, should be examined. It might even be worthwhile to investigate the usage of the ratios in other substrates in determining the number of layers.

# References


[1] Bae, S., Kim, H., Lee, Y., Xu, X., Park, J.-S., Zheng, Y., Balakrishnan, J., Lei, T., Kim, H. R., Song, Y. I., et al. Roll-to-roll production of 30-inch graphene films for transparent electrodes. Nat. Nanotechnol. **5** (2010), 574–578.

[2] Balandin, A. A., Ghosh, S., Bao, W., Calizo, I., Teweldebrhan, D., Miao, F., and Lau, C. N. Superior thermal conductivity of single-layer graphene. Nano Lett. **8** (2008), 902–907.

[3] Baskin, Y., and Meyer, L. Lattice constants of graphite at low temperatures. Phys. Rev. **100** (1955), 544.

[4] Bolotin, K. I., Sikes, K., Jiang, Z., Klima, M., Fudenberg, G., Hone, J., Kim, P., and Stormer, H. Ultrahigh electron mobility in suspended graphene. Solid State Commun. **146** (2008), 351–355.

[5] Buzzi-Ferraris, G., and Manenti, F. Outlier detection in large data sets. Comput. Chem. Eng. **35** (2011), 388–390.

[6] Calizo, I., Ghosh, S., Bao, W., Miao, F., Lau, C. N., and Balandin, A. A. Raman nanometrology of graphene: Temperature and substrate effects. Solid State Commun. **149** (2009), 1132–1135.

[7] Carvalho, B. R., Hao, Y., Righi, A., Rodriguez-Nieva, J. F., Colombo, L., Ruoff, R. S., Pimenta, M. A., and Fantini, C. Probing carbon isotope effects on the Raman spectra of graphene with different $^{13}$C concentrations. Phys. Rev. B **92** (2015), 125406.

[8] Casiraghi, C., Hartschuh, A., Lidorikis, E., Qian, H., Harutyunyan, H., Gokus, T., Novoselov, K., and Ferrari, A. Rayleigh imaging of graphene and graphene layers. Nano Lett. **7** (2007), 2711–2717.

[9] Casiraghi, C., Hartschuh, A., Qian, H., Piscanec, S., Georgi, C., Fasoli, A., Novoselov, K., Basko, D., and Ferrari, A. Raman spectroscopy of graphene edges. Nano Lett. **9** (2009), 1433–1441.

[10] Casiraghi, C., Pisana, S., Novoselov, K., Geim, A., and Ferrari, A. Raman fingerprint of charged impurities in graphene. Appl. Phys. Lett. **91** (2007), 233108.

[11] Chen, Y.-F., Liu, D., Wang, Z.-G., Li, P.-J., Hao, X., Cheng, K., Fu, Y., Huang, L.-X., Liu, X.-Z., Zhang, W.-L., et al. Rapid determination of the thickness of graphene using the ratio of color difference. J. Phys. Chem. C **115** (2011), 6690–6693.

[12] Cheon, S., Kihm, K. D., goo Kim, H., Lim, G., Park, J. S., and Lee, J. S. How to reliably determine the complex refractive index (RI) of graphene by using two independent measurement constraints. Sci. Rep. **4** (2014).

[13] Cheon, S., Kihm, K. D., Park, J. S., Lee, J. S., Lee, B. J., Kim, H., and Hong, B. H. How to optically count graphene layers. Opt. Lett. **37** (2012), 3765–3767.

[14] Chiu, C.-W., Chen, S.-C., Huang, Y.-C., Shyu, F.-L., and Lin, M.-F. Critical optical properties of AA-stacked multilayer graphenes. Appl. Phys. Lett. **103** (2013), 041907.

[15] Cong, C., Li, K., Zhang, X. X., and Yu, T. Visualization of arrangements of carbon atoms in graphene layers by Raman mapping and atomic-resolution TEM. Sci. Rep. **3** (2013).

[16] Cong, C., and Yu, T. Evolution of Raman G and G' (2D) modes in folded graphene layers. Phys. Rev. B **89** (2014), 235430.

[17] Cong, C., Yu, T., Saito, R., Dresselhaus, G. F., and Dresselhaus, M. S. Second-order overtone and combination Raman modes of graphene layers in the range of 1690–2150 $cm^{-1}$. ACS Nano **5** (2011), 1600–1605.

[18] Cong, C., Yu, T., Sato, K., Shang, J., Saito, R., Dresselhaus, G. F., and Dresselhaus, M. S. Raman characterization of ABA- and ABC-stacked trilayer graphene. ACS Nano **5** (2011), 8760–8768.

[19] Cooper, D. R., D'Anjou, B., Ghattamaneni, N., Harack, B., Hilke, M., Horth, A., Majlis, N., Massicotte, M., Vandsburger, L., Whiteway, E., et al. Experimental review of graphene. ISRN Condensed Matter Physics **2012** (2012).

[20] Coraux, J., N'Diaye, A. T., Busse, C., and Michely, T. Structural coherency of graphene on Ir(111). Nano Lett. **8** (2008), 565–570.

[21] Das, A., Pisana, S., Chakraborty, B., Piscanec, S., Saha, S., Waghmare, U., Novoselov, K., Krishnamurthy, H., Geim, A., Ferrari, A., et al. Monitoring dopants by Raman scattering in an electrochemically top-gated graphene transistor. Nat. Nanotechnol. **3** (2008), 210–215.

[22] Denis, P. A. Band gap opening of monolayer and bilayer graphene doped with aluminium, silicon, phosphorus, and sulfur. Chem. Phys. Lett. **492** (2010), 251–257.

[23] Djurišić, A. B., and Li, E. H. Optical properties of graphite. J. Appl. Phys. **85** (1999), 7404–7410.

[24] Eckmann, A., Felten, A., Mishchenko, A., Britnell, L., Krupke, R., Novoselov, K. S., and Casiraghi, C. Probing the nature of defects in graphene by Raman spectroscopy. Nano Lett. **12** (2012), 3925–3930.

[25] Ek-Weis, J., Costa, S., Frank, O., and Kalbac, M. Heating isotopically labeled bernal stacked graphene: A Raman spectroscopy study. J. Phys. Chem. Lett. **5** (2014), 549–554.

[26] El-Gohary, S. H., Kim, N.-H., and Byun, K. M. Optical determination of thick graphene layer number based on surface plasmon resonance. J. Nanophotonics **7** (2013), 073799.

[27] Elias, D., Nair, R., Mohiuddin, T., Morozov, S., Blake, P., Halsall, M., Ferrari, A., Boukhvalov, D., Katsnelson, M., Geim, A., et al. Control of graphene's properties by reversible hydrogenation: Evidence for graphane. Science **323** (2009), 610–613.

[28] Emtsev, K. V., Bostwick, A., Horn, K., Jobst, J., Kellogg, G. L., Ley, L., McChesney, J. L., Ohta, T., Reshanov, S. A., Röhrl, J., et al. Towards wafer-size graphene layers by atmospheric pressure graphitization of silicon carbide. Nat. Mater. **8** (2009), 203–207.

[29] Ferrari, A. C., and Basko, D. M. Raman spectroscopy as a versatile tool for studying the properties of graphene. Nat. Nanotechnol. **8** (2013), 235–246.

[30] Ferrari, A. C., Bonaccorso, F., Fal'ko, V., Novoselov, K. S., Roche, S., Bøggild, P., Borini, S., Koppens, F. H., Palermo, V., Pugno, N., et al. Science and technology roadmap for graphene, related two-dimensional crystals, and hybrid systems. Nanoscale **7** (2015), 4598–4810.

[31] Gao, L., Ren, W., Li, F., and Cheng, H.-M. Total color difference for rapid and accurate identification of graphene. ACS Nano **2** (2008), 1625–1633.

[32] Geim, A. K. Graphene: Status and prospects. Science **324** (2009), 1530–1534.

[33] Geim, A. K., and Novoselov, K. S. The rise of graphene. Nat. Mater. **6** (2007), 183–191.

[34] Graf, D., Molitor, F., Ensslin, K., Stampfer, C., Jungen, A., Hierold, C., and Wirtz, L. Spatially resolved Raman spectroscopy of single- and few-layer graphene. Nano Lett. **7** (2007), 238–242.

[35] Gray, A., Balooch, M., Allegret, S., Gendt, S. D., and Wang, W.-E. Optical detection and characterization of graphene by broadband spectrophotometry. J. Appl. Phys. **104** (2008), 053109.

[36] Gupta, A., Chen, G., Joshi, P., Tadigadapa, S., and Eklund, P. Raman scattering from high-frequency phonons in supported n-graphene layer films. Nano Lett. **6** (2006), 2667–2673.

[37] Han, W., Kawakami, R. K., Gmitra, M., and Fabian, J. Graphene spintronics. Nat. Nanotechnol. **9** (2014), 794–807.

[38] Hao, Y., Wang, Y., Wang, L., Ni, Z., Wang, Z., Wang, R., Koo, C. K., Shen, Z., and Thong, J. T. Probing layer number and stacking order of few-layer graphene by Raman spectroscopy. Small **6** (2010), 195–200.

[39] Havener, R. W., Zhuang, H., Brown, L., Hennig, R. G., and Park, J. Angle-resolved Raman imaging of interlayer rotations and interactions in twisted bilayer graphene. Nano Lett. **12** (2012), 3162–3167.

[40] Heerema, S. J., and Dekker, C. Graphene nanodevices for DNA sequencing. Nat. Nanotechnol. **11** (2016), 127–136.

[41] Heller, E. J., Yang, Y., Kocia, L., Chen, W., Fang, S., Borunda, M., and Kaxiras, E. Theory of graphene Raman scattering. ACS Nano **10** (2016), 2803–2818.

[42] Herziger, F., and Maultzsch, J. Influence of the layer number and stacking order on out-of-plane phonons in few-layer graphene. Phys. Status Solidi B **250** (2013), 2697–2701.

[43] Herziger, F., May, P., and Maultzsch, J. Layer-number determination in graphene by out-of-plane phonons. Phys. Rev. B **85** (2012), 235447.

[44] Hiura, H., Miyazaki, H., and Tsukagoshi, K. Determination of the number of graphene layers: Discrete distribution of the secondary electron intensity stemming from individual graphene layers. Appl. Phys Express **3** (2010), 095101.

[45] Hu, S., Lozada-Hidalgo, M., Wang, F., Mishchenko, A., Schedin, F., Nair, R., Hill, E., Boukhvalov, D., Katsnelson, M., Dryfe, R., et al. Proton transport through one-atom-thick crystals. Nature **516** (2014), 227–230.

[46] Hwang, J.-S., Lin, Y.-H., Hwang, J.-Y., Chang, R., Chattopadhyay, S., Chen, C.-J., Chen, P., Chiang, H.-P., Tsai, T.-R., Chen, L.-C., et al. Imaging layer number and stacking order through formulating Raman fingerprints obtained from hexagonal single crystals of few layer graphene. Nanotechnology **24** (2013), 015702.

[47] Hwangbo, Y., Lee, C.-K., Mag-Isa, A. E., Jang, J.-W., Lee, H.-J., Lee, S.-B., Kim, S.-S., and Kim, J.-H. Interlayer non-coupled optical properties for determining the number of layers in arbitrarily stacked multilayer graphenes. Carbon **77** (2014), 454–461.

[48] Jellison Jr, G. E., Hunn, J. D., and Lee, H. N. Measurement of optical functions of highly oriented pyrolytic graphite in the visible. Phys. Rev. B **76** (2007), 085125.

[49] Jorio, A. Raman spectroscopy in graphene-based systems: Prototypes for nanoscience and nanometrology. ISRN Nanotechnology **2012** (2012).

[50] Jung, I., Pelton, M., Piner, R., Dikin, D. A., Stankovich, S., Watcharotone, S., Hausner, M., and Ruoff, R. S. Simple approach for high-contrast optical imaging and characterization of graphene-based sheets. Nano Lett. **7** (2007), 3569–3575.

[51] Kim, H., Park, K.-Y., Hong, J., and Kang, K. All-graphene-battery: Bridging the gap between supercapacitors and lithium ion batteries. Sci. Rep. **4** (2014).

[52] Kim, K., Coh, S., Tan, L. Z., Regan, W., Yuk, J. M., Chatterjee, E., Crommie, M., Cohen, M. L., Louie, S. G., and Zettl, A. Raman spectroscopy study of rotated double-layer graphene: Misorientation-angle dependence of electronic structure. Phys. Rev. Lett. **108** (2012), 246103.

[53] Klintenberg, M., Ortiz, C., Sanyal, B., Fransson, J., Eriksson, O., et al. Evolving properties of two-dimensional materials: From graphene to graphite. J. Phys.: Condens. Matter **21** (2009), 335502.

[54] Kochat, V., Pal, A. N., Sneha, E., Sampathkumar, A., Gairola, A., Shivashankar, S., Raghavan, S., and Ghosh, A. High contrast imaging and thickness determination of graphene with in-column secondary electron microscopy. J. Appl. Phys. **110** (2011), 014315.

[55] Koenig, S. P., Boddeti, N. G., Dunn, M. L., and Bunch, J. S. Ultrastrong adhesion of graphene membranes. Nat. Nanotechnol. **6** (2011), 543–546.

[56] Koh, Y. K., Bae, M.-H., Cahill, D. G., and Pop, E. Reliably counting atomic planes of few-layer graphene (n > 4). ACS Nano **5** (2010), 269–274.

[57] Kontis, C., Mueller, M. R., Kuechenmeister, C., Kallis, K. T., and Knoch, J. Optimizing the identification of mono- and bilayer graphene on multilayer substrates. Appl. Opt. **51** (2012), 385–389.

[58] Kravets, V., Grigorenko, A., Nair, R., Blake, P., Anissimova, S., Novoselov, K., and Geim, A. Spectroscopic ellipsometry of graphene and an exciton-shifted van Hove peak in absorption. Phys. Rev. B **81** (2010), 155413.

[59] Lee, C., Wei, X., Kysar, J. W., and Hone, J. Measurement of the elastic properties and intrinsic strength of monolayer graphene. Science **321** (2008), 385–388.

[60] Li, H., Wu, J., Huang, X., Lu, G., Yang, J., Lu, X., Xiong, Q., and Zhang, H. Rapid and reliable thickness identification of two-dimensional nanosheets using optical microscopy. ACS Nano **7** (2013), 10344–10353.

[61] Li, X.-L., Qiao, X.-F., Han, W.-P., Lu, Y., Tan, Q.-H., Liu, X.-L., and Tan, P.-H. Layer number identification of intrinsic and defective multilayered graphenes up to 100 layers by the Raman mode intensity from substrates. Nanoscale **7** (2015), 8135–8141.

[62] Lotya, M., Hernandez, Y., King, P. J., Smith, R. J., Nicolosi, V., Karlsson, L. S., Blighe, F. M., De, S., Wang, Z., McGovern, I., et al. Liquid phase production of graphene by exfoliation of graphite in surfactant/water solutions. J. Am. Chem. Soc. **131** (2009), 3611–3620.

[63] Lucchese, M. M., Stavale, F., Ferreira, E. M., Vilani, C., Moutinho, M., Capaz, R. B., Achete, C., and Jorio, A. Quantifying ion-induced defects and Raman relaxation length in graphene. Carbon **48** (2010), 1592–1597.

[64] Lui, C. H., and Heinz, T. F. Measurement of layer breathing mode vibrations in few-layer graphene. Phys. Rev. B **87** (2013), 121404.

[65] Lui, C. H., Li, Z., Chen, Z., Klimov, P. V., Brus, L. E., and Heinz, T. F. Imaging stacking order in few-layer graphene. Nano Lett. **11** (2010), 164–169.

[66] Lui, C. H., Malard, L. M., Kim, S., Lantz, G., Laverge, F. E., Saito, R., and Heinz, T. F. Observation of layer-breathing mode vibrations in few-layer graphene through combination Raman scattering. Nano Lett. **12** (2012), 5539–5544.

[67] Malard, L., Pimenta, M., Dresselhaus, G., and Dresselhaus, M. Raman spectroscopy in graphene. Phys. Rep. **473** (2009), 51–87.

[68] Matković, A., Ralević, U., Chhikara, M., Jakovljević, M. M., Jovanović, D., Bratina, G., and Gajić, R. Influence of transfer residue on the optical properties of chemical vapor deposited graphene investigated through spectroscopic ellipsometry. J. Appl. Phys. **114** (2013), 093505.

[69] Matković, A., Ralević, U., Isić, G., Jakovljević, M., Vasić, B., Milošević, I., Marković, D., and Gajić, R. Spectroscopic ellipsometry and the Fano resonance modeling of graphene optical parameters. Phys. Scr. **2012** (2012), 014069.

[70] Mohiuddin, T., Lombardo, A., Nair, R., Bonetti, A., Savini, G., Jalil, R., Bonini, N., Basko, D., Galiotis, C., Marzari, N., et al. Uniaxial strain in graphene by Raman spectroscopy: G peak splitting, Grüneisen parameters, and sample orientation. Phys. Rev. B **79** (2009), 205433.

[71] Moon, P., and Koshino, M. Optical absorption in twisted bilayer graphene. Phys. Rev. B **87** (2013), 205404.

[72] Müller, M., Gumprich, A., Ecik, E., Kallis, K., Winkler, F., Kardynal, B., Petrov, I., Kunze, U., and Knoch, J. Visibility of two-dimensional layered materials on various substrates. J. Appl. Phys. **118** (2015), 145305.

[73] Na, M. Y., Lee, S.-M., Kim, D. H., and Chang, H. J. Dark-field transmission electron microscopy imaging technique to visualize the local structure of two-dimensional material; graphene. Applied Microscopy **45** (2015), 23–31.

[74] Nair, R., Blake, P., Grigorenko, A., Novoselov, K., Booth, T., Stauber, T., Peres, N., and Geim, A. Fine structure constant defines visual transparency of graphene. Science **320** (2008), 1308–1308.

[75] Nakada, K., Fujita, M., Dresselhaus, G., and Dresselhaus, M. S. Edge state in graphene ribbons: Nanometer size effect and edge shape dependence. Phys. Rev. B **54** (1996), 17954.

[76] Nelson, F., Kamineni, V., Zhang, T., Comfort, E., Lee, J., and Diebold, A. Optical properties of large-area polycrystalline chemical vapor deposited graphene by spectroscopic ellipsometry. Appl. Phys. Lett. **97** (2010), 253110.

[77] Nemes-Incze, P., Osváth, Z., Kamarás, K., and Biró, L. Anomalies in thickness measurements of graphene and few layer graphite crystals by tapping mode atomic force microscopy. Carbon **46** (2008), 1435–1442.

[78] Nguyen, T. A., Lee, J.-U., Yoon, D., Cheong, H., et al. Excitation energy dependent Raman signatures of ABA- and ABC-stacked few-layer graphene. Sci. Rep. **4** (2014).

[79] Ni, Z., Wang, H., Kasim, J., Fan, H., Yu, T., Wu, Y., Feng, Y., and Shen, Z. Graphene thickness determination using reflection and contrast spectroscopy. Nano Lett. **7** (2007), 2758–2763.

[80] Novoselov, K. S. Graphene: Materials in the flatland (Nobel Lecture). Angew. Chem. Int. Ed. **50** (2011), 6986–7002.

[81] Ochoa-Martínez, E., Gabás, M., Barrutia, L., Pesquera, A., Centeno, A., Palanco, S., Zurutuza, A., and Algora, C. Determination of a refractive index and an extinction coefficient of standard production of CVD-graphene. Nanoscale **7** (2015), 1491–1500.

[82] Orfanidis, S. J. *Electromagnetic waves and antennas*. Rutgers University New Brunswick, NJ, 2014.

[83] Palik, E. D. *Handbook of optical constants of solids*, vol. 3. Academic press, 1998.

[84] Ping, J., and Fuhrer, M. S. Layer number and stacking sequence imaging of few-layer graphene by transmission electron microscopy. Nano Lett. **12** (2012), 4635–4641.

[85] Prasai, D., Tuberquia, J. C., Harl, R. R., Jennings, G. K., and Bolotin, K. I. Graphene: Corrosion-inhibiting coating. ACS Nano **6** (2012), 1102–1108.

[86] Rao, R., Podila, R., Tsuchikawa, R., Katoch, J., Tishler, D., Rao, A. M., and Ishigami, M. Effects of layer stacking on the combination Raman modes in graphene. ACS Nano **5** (2011), 1594–1599.

[87] Robinson, J. T., Schmucker, S. W., Diaconescu, C. B., Long, J. P., Culbertson, J. C., Ohta, T., Friedman, A. L., and Beechem, T. E. Electronic hybridization of large-area stacked graphene films. ACS Nano **7** (2012), 637–644.

[88] Rycerz, A., Tworzydło, J., and Beenakker, C. Valley filter and valley valve in graphene. Nat. Phys. **3** (2007), 172–175.

[89] Santoso, I., Singh, R. S., Gogoi, P. K., Asmara, T. C., Wei, D., Chen, W., Wee, A. T., Pereira, V. M., and Rusydi, A. Tunable optical absorption and interactions in graphene via oxygen plasma. Phys. Rev. B **89** (2014), 075134.

[90] Schedin, F., Geim, A., Morozov, S., Hill, E., Blake, P., Katsnelson, M., and Novoselov, K. Detection of individual gas molecules adsorbed on graphene. Nat. Mater. **6** (2007), 652–655.

[91] Schönherr, H., and Vancso, G. J. *Scanning force microscopy of polymers*. Springer, 2010.

[92] Shibuta, Y., and Elliott, J. A. Interaction between two graphene sheets with a turbostratic orientational relationship. Chem. Phys. Lett. **512** (2011), 146–150.

[93] Surwade, S. P., Smirnov, S. N., Vlassiouk, I. V., Unocic, R. R., Veith, G. M., Dai, S., and Mahurin, S. M. Water desalination using nanoporous single-layer graphene. Nat. Nanotechnol. **10** (2015), 459–464.

[94] Tan, P., Han, W., Zhao, W., Wu, Z., Chang, K., Wang, H., Wang, Y., Bonini, N., Marzari, N., Pugno, N., et al. The shear mode of multilayer graphene. Nat. Mater. **11** (2012), 294–300.

[95] Tassin, P., Koschny, T., and Soukoulis, C. M. Graphene for terahertz applications. Science **341** (2013), 620–621.

[96] Tsurumi, J., Saito, Y., and Verma, P. Evaluation of the interlayer interactions of few layers of graphene. Chem. Phys. Lett. **557** (2013), 114–117.

[97] Wang, H., Wang, Y., Cao, X., Feng, M., and Lan, G. Vibrational properties of graphene and graphene layers. J. Raman Spectrosc. **40** (2009), 1791–1796.

[98] Weber, J., Calado, V., and Van de Sanden, M. Optical constants of graphene measured by spectroscopic ellipsometry. Appl. Phys. Lett. **97** (2010), 091904.

[99] Wu, T., Zhang, X., Yuan, Q., Xue, J., Lu, G., Liu, Z., Wang, H., Wang, H., Ding, F., Yu, Q., et al. Fast growth of inch-sized single-crystalline graphene from a controlled single nucleus on Cu-Ni alloys. Nat. Mater. **15** (2016), 43–47.

[100] Wu, Y., Lin, Y.-m., Bol, A. A., Jenkins, K. A., Xia, F., Farmer, D. B., Zhu, Y., and Avouris, P. High-frequency, scaled graphene transistors on diamond-like carbon. Nature **472** (2011), 74–78.

[101] Yoon, D., Moon, H., Son, Y.-W., Choi, J. S., Park, B. H., Cha, Y. H., Kim, Y. D., and Cheong, H. Interference effect on Raman spectrum of graphene on $SiO_2$/Si. Phys. Rev. B **80** (2009), 125422.

[102] Yoon, D., Son, Y.-W., and Cheong, H. Strain-dependent splitting of the double-resonance Raman scattering band in graphene. Phys. Rev. Lett. **106** (2011), 155502.

[103] You, Y., Ni, Z., Yu, T., and Shen, Z. Edge chirality determination of graphene by Raman spectroscopy. Appl. Phys. Lett. **93** (2008), 163112.

[104] Yu, G., Gorbachev, R., Tu, J., Kretinin, A., Cao, Y., Jalil, R., Withers, F., Ponomarenko, L., Piot, B., Potemski, M., et al. Hierarchy of Hofstadter states and replica quantum Hall ferromagnetism in graphene superlattices. Nat. Phys. **10** (2014), 525–529.

[105] Zan, R., Ramasse, Q. M., Bangert, U., and Novoselov, K. S. Graphene reknits its holes. Nano Lett. **12** (2012), 3936–3940.

[106] Zhang, X., Han, W.-P., Qiao, X.-F., Tan, Q.-H., Wang, Y.-F., Zhang, J., and Tan, P.-H. Raman characterization of AB- and ABC-stacked few-layer graphene by interlayer shear modes. Carbon **99** (2016), 118–122.

[107] Zhang, Y., Tang, T.-T., Girit, C., Hao, Z., Martin, M. C., Zettl, A., Crommie, M. F., Shen, Y. R., and Wang, F. Direct observation of a widely tunable bandgap in bilayer graphene. Nature **459** (2009), 820–823.

# Appendix A

# Figures

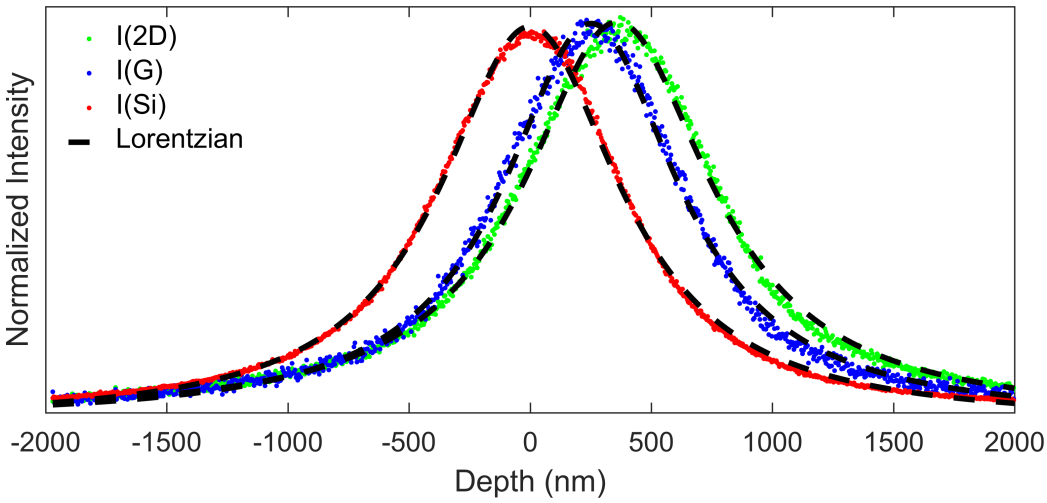


Figure A.1: Measured Raman intensity depth profiles for the Si-peak (red), the G-peak (blue), and the 2D-peak (green) through BLG on Si with 285 nm $SiO_2$. Dashed lines are the fitted Lorentzian lineshapes, which are expected for Raman signals through a pinhole originating from an ideal Gaussian laser beam. The average Rayleigh length, $z_R = 453.3$ nm is ideally half the FWHM and is a typical value for 532 nm laser beam focused through 100× lens (NA 0.95). The profile offsets, 251.6 nm for G and 360.1 nm for 2D, are attributed to be caused by differences in unique interference patterns for each peak because 1) Si-peak originates physically from different location than the graphene peaks, and 2) each peak differs in scattering wavelength.

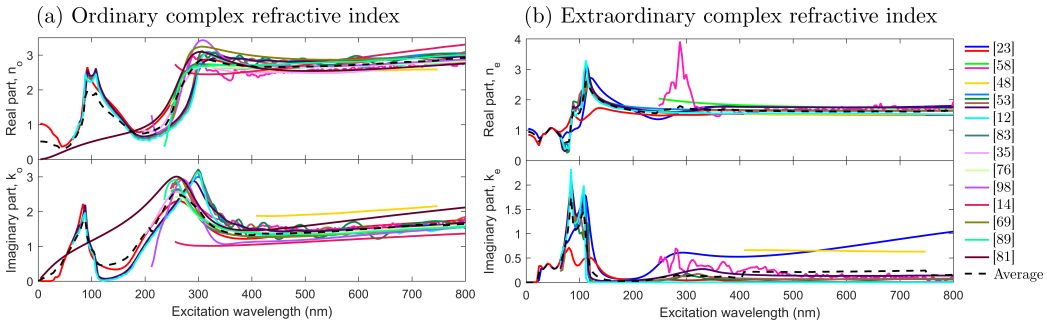


Figure A.2: Real and imaginary parts of the graphene complex refractive indices for datasets from various sources, including the weighted average as dashed black line, which is depicted more clearly in Figure 4.5. Left panel is for (a) ordinary waves and right for (b) extraordinary waves.

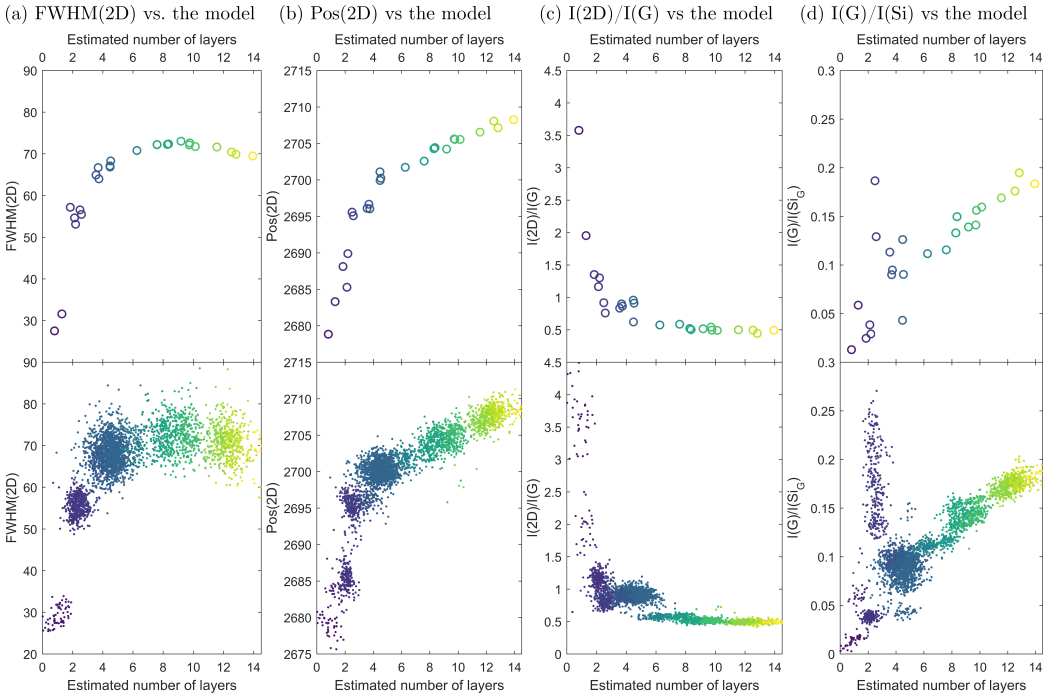


Figure A.3: Number of graphene layers obtained via the Si-peak analysis for pristine graphene on 365 nm $SiO_2$/Si–substrate correlated with four well known Raman layer-number fingerprints in determining the number of layers: a) FWHM(2D), b) Pos(2D), c) Ratio–I(2D, G) and d) Ratio–I(G, $Si_G$). The plots on top depict the area-averaged values in samples. The plots on bottom represent the raw pixel-to-pixel correlation. The data colouring corresponds to the number of layers: the lighter the shade, the thicker the graphene. This comparison is equivalent to that of 285 nm in Figure 5.2.